Communications in Analysis and Mechanics

https://www.aimspress.com/journal/cam

Communications in Analysis and Mechanics, 18(1): 142–171.
DOI: 10.3934/cam.2026006
Received: 25 July 2025
Revised: 15 October 2025
Accepted: 04 January 2026
Published: 28 February 2026

Research article

Inversion of two-dimensional Fresnel experimental dataset using orthogonality sampling method with single and multiple sources: the case of transverse magnetic polarized waves

Won-Kwang Park*

Department of Information Security, Cryptography, and Mathematics, Kookmin University, Seoul, 02707, Korea

* **Correspondence:** Email: parkwk@kookmin.ac.kr.

Abstract: This paper considers the application of the orthogonality sampling method (OSM) with single and multiple sources for a fast identification of small objects in the limited-aperture inverse scattering problem. First, we apply the OSM with a single source and demonstrate that the indicator function of the OSM with a single source can be expressed by the Bessel function of order zero of the first kind, an infinite series of Bessel functions of nonzero integer order of the first kind, the range of the signal receiver, and the emitter location. We then explain that the objects can be identified using the OSM with a single source; however, the identification is strongly influenced by the location of the source and the applied frequency. To realize effective improvement, we consider the OSM with multiple sources. Based on the identified structure of the OSM with a single source, we propose an indicator function for the OSM with multiple sources and demonstrate that it can be expressed by the square of the Bessel function of order zero of the first kind and an infinite series of the square of the Bessel function of nonzero integer order of the first kind. This result shows that the locations of objects can be uniquely identified using the designed OSM. Simulation results with experimental data provided by the Institute Fresnel demonstrate the advantages and disadvantages of the OSM with a single source and how the proposed OSM with multiple sources behaves.

Keywords: orthogonality sampling method; limited-aperture inverse scattering problem; Bessel functions of the first kind; Fresnel experimental data
Mathematics Subject Classification: 78A46

1. Introduction

The development of an effective and stable technique to retrieve unknown objects from a measured scattered field or scattering parameter data is an old but interesting research subject because it is strongly

related to modern human life, e.g., biomedical imaging [1, 2], including breast cancer detection [3, 4], through-wall imaging for defect recognition [5, 6], damage detection in concrete structures [7, 8], land mine detection [9, 10], synthetic-aperture radar imaging [11–13], ground penetrating radar [14, 15], and artificial intelligence techniques [16–19]. Note that most related algorithms are based on Newton-type iteration schemes; thus, a good initial guess that is sufficiently close to the unknown objects must be generated and applied at the beginning of the iteration process. We refer to [20, 21] for related discussions.

Rather than iterative-based algorithms, alternative non-iterative techniques have been investigated to retrieve unknown objects. Different studies on the bifocusing method [22–24], the direct sampling method [25–27], the factorization method [28–30], MUltiple SIgnal Classification (MUSIC) [31–33], Kirchhoff and subspace migration techniques [34–36], and topological derivatives [37–39] have shown that, although complete information of the objects, e.g., material properties, cannot be retrieved, these are very effective techniques to identify the existence, location, and outline shape of objects.

The orthogonality sampling method (OSM) is a non-iterative imaging technique for both the inverse scattering problem and microwave imaging. Since its initial proposal by Potthast [40], the OSM has been applied to various inverse scattering problems, for example, imaging of unknown objects with multi-frequency OSM [41], detection of crack-like objects in limited-aperture inverse acoustic problems [42], and retrieval of three-dimensional arbitrary shaped objects [43]. Throughout these studies, it is confirmed that the OSM is a very fast, stable, and effective imaging technique in various inverse scattering problems. However, most of these studies performed numerical simulations to demonstrate the effectiveness of the OSM on synthetic data. In other studies [44, 45], the OSM was applied to real-world inverse scattering problems using an experimental database produced by the Institute Fresnel, France [46, 47]. The OSM has demonstrated both applicability and robustness for the retrieval of a set of small objects from experimental data. However, an appropriate mathematical theory that explains certain phenomena such as ① why the imaging performance significantly depends on the source location, ② why the use of low and high frequencies is inappropriate for retrieving multiple objects, and ③ why the locations of the objects can be uniquely identified using multiple sources as well as an alternative technique to improve imaging performance has not yet been established.

In this paper, we consider the application of the OSM to identify a set of objects from experimental data. First, we introduce the traditional indicator function for the OSM with a single source and reveal its mathematical structure by establishing a relationship with the Bessel function of order zero of the first kind, an infinite series of Bessel functions of nonzero integer order of the first kind, the range of the signal receiver, and the emitter location. Based on this structure, we explain some intrinsic properties of the OSM and provide theoretical answers to the above mentioned unexplained phenomena. Then, we present the results of a simulation performed on experimental data to demonstrate the theoretical result and fundamental limitation of object detection.

We then consider the OSM with multiple sources to improve the imaging performance for proper detection of objects. Here, instead of the traditional indicator function with multiple sources introduced in a previous study [40], we propose a new indicator function of the OSM. To demonstrate the applicability, effectiveness, and improvement of the proposed indicator function and its unique determination of small objects, we show that it can be expressed by the square of the Bessel function of order zero of the first kind and an infinite series of the square of the Bessel function of nonzero integer order of the first kind. We then present simulation results to support the established structure and the discovered certain properties of the proposed indicator function, and we compare the imaging and detection performance.

The remainder of this paper is organized as follows: In Section 2, we briefly survey the direct scattering problem in the presence of a set of small objects, and we introduce the traditional indicator function of the OSM. In Section 3, the mathematical structure of the indicator function with a single source is investigated by establishing a relationship with an infinite series of Bessel functions, a range of receivers, and the emitter location. Then, in Section 4, simulation results obtained on the synthetic data and Fresnel experimental database are presented to confirm the theoretical result and examine the influence of the emitter location and the frequencies at operation. In Section 5, we introduce the traditional indicator function and propose another indicator function with multiple sources. We also establish the mathematical structure and discuss some of the intrinsic properties of the proposed indicator function. In Section 6, we present relevant simulation results with synthetic and Fresnel experimental database. Finally, the paper is concluded in Section 7, including a summary of potential future research perspectives.

2. Direct scattering problem and orthogonality sampling method

Let Ω be a two-dimensional homogeneous region, let $D_s \subset \Omega$, $s = 1, 2, \ldots, S$ be a two-dimensional small object with smooth boundary ∂D_s, and let D be the collection of D_s. In this paper, we assume that all D_s are well-separated and Ω is a subset of the interior of an anechoic chamber such that the background conductivity, permeability, and permittivity values are set to $\sigma_0 \approx 0$, $\mu_0 = 4\pi \times 10^{-7}\,\mathrm{H/m}$, and $\varepsilon_0 = 8.854 \times 10^{-12}\,\mathrm{F/m}$, respectively. Refer to the literature for additional details [48]. Here, each D_s and Ω is characterized by the dielectric permittivity value at the given angular frequency $\omega = 2\pi f$. Let ε_s and ε_0 be the permittivity values of D_s and Ω, respectively, and let $k_\mathrm{b} = \omega\sqrt{\varepsilon_0\mu_0}$ be the background wavenumber and $\lambda > 0$ denote the wavelength. Given the above, we introduce the following piecewise constant:

$$\varepsilon(\mathbf{r}) = \begin{cases} \varepsilon_s & \text{for} \quad \mathbf{r} \in D_s, \\ \varepsilon_0 & \text{for} \quad \mathbf{r} \in \Omega \backslash \overline{D}. \end{cases}$$

We denote $\mathbf{a}_m$ and $\mathbf{b}_{m,n}$ as the location of the mth emitter $\mathcal{A}_m$, $m = 1, 2, \ldots, M$ and corresponding nth receiver $\mathcal{B}_{m,n}$, $n = 1, 2, \ldots, N$, respectively. Following the literature [46], all $\mathbf{a}_m$ and $\mathbf{b}_{m,n}$ are located outside Ω and can be expressed as follows:

$$\mathbf{a}_m = |\mathbf{a}_m|(\cos\vartheta_m, \sin\vartheta_m) = |\mathbf{a}_m|\boldsymbol{\vartheta}_m \quad \text{with} \quad |\mathbf{a}_m| \equiv |\mathbf{a}| = 0.72\,\mathrm{m}, \quad \vartheta_m = \frac{2(m-1)\pi}{M}$$

and

$$\mathbf{b}_{m,n} = |\mathbf{b}_{m,n}|(\cos\theta_{m,n}, \sin\theta_{m,n}) = |\mathbf{b}_{m,n}|\boldsymbol{\theta}_{m,n} \quad \text{with} \quad |\mathbf{b}_{m,n}| \equiv |\mathbf{b}| = 0.76\,\mathrm{m}, \quad \theta_{m,n} = \vartheta_m + \frac{\pi}{3} + \frac{4(n-1)\pi}{3(N-1)},$$

respectively. Here, $\boldsymbol{\vartheta}_m \in \mathbb{S}^1$ and $\boldsymbol{\theta}_{m,n} \in \mathbb{S}^1_m$, where $\mathbb{S}^1$ denotes the unit circle centered at the origin, and

$$\mathbb{S}^1_m = \left\{(\cos\theta, \sin\theta) : \vartheta_m + \frac{\pi}{3} \le \theta \le \vartheta_m + \frac{5\pi}{3}\right\} \subset \mathbb{S}^1.$$

For an illustration, refer to Figure 1. Accordingly, the incident field generated by a fixed-point source $\mathcal{A}_m$ is given by

$$u_\mathrm{inc}(\mathbf{r}, \mathbf{a}_m) = G(\mathbf{r}, \mathbf{a}_m) = -\frac{i}{4}H_0^{(1)}(k_\mathrm{b}|\mathbf{r} - \mathbf{a}_m|), \quad \mathbf{r} \in \Omega,$$

where $H_0^{(1)}$ denotes the Hankel function of order zero of the first kind. We denote by $u(\cdot, \mathbf{r})$ the time-harmonic total field in the presence of D, which satisfies

$$\triangle u(\cdot, \mathbf{r}) + \omega^2 \mu_0 \varepsilon(\mathbf{r}) u(\cdot, \mathbf{r}) = 0 \quad \text{for} \quad \mathbf{r} \in \Omega$$

with the transmission condition $u(\cdot, \mathbf{r})\big|_- - u(\cdot, \mathbf{r})\big|_+ = 0$ on ∂D_s, $s = 1, 2, \ldots, S$. Here, the time harmonic $e^{-i\omega t}$ is assumed.

Let $u_{\text{scat}}(\mathbf{b}_{m,n}, \mathbf{a}_m)$ denote the scattered field measured at $\mathcal{B}_{m,n}$ due to the incident field $u_{\text{inc}}(\mathbf{r}, \mathbf{a}_m)$. Then, u_{scat} can be represented as a single-layer potential involving an unknown density function φ [49]:

$$u_{\text{scat}}(\mathbf{b}_{m,n}, \mathbf{a}_m) = u(\mathbf{b}_{m,n}, \mathbf{r}) - u_{\text{inc}}(\mathbf{r}, \mathbf{a}_m) = \int_D G(\mathbf{b}_{m,n}, \mathbf{r}) \varphi(\mathbf{r}, \mathbf{a}_m) \mathrm{d}\mathbf{r}.$$

Note that the closed form of the density function $\varphi(\mathbf{r}, \mathbf{a}_m)$ is unknown; thus, it is inappropriate to employ $u_{\text{scat}}(\mathbf{b}_{m,n}, \mathbf{a}_m)$ directly to design the indicator function of the OSM. Due to this reason, we use the following integral equation formula [50], which is the key formula to design and analyze the structure of the indicator function.

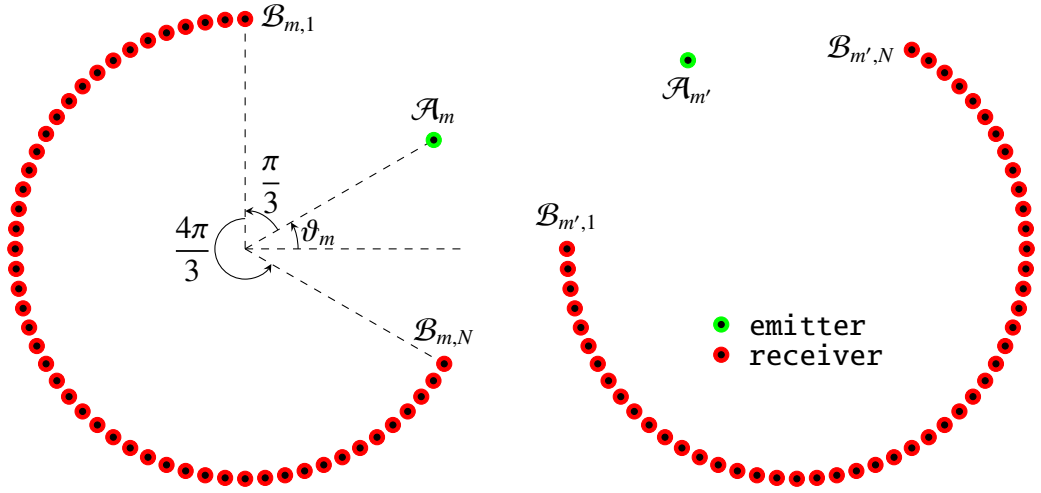

Figure 1. Receiver arrangements corresponding to the emitter location.

Remark 2.1 (Born approximation and integral equation formula). Let $\text{diam}(D_s)$ denote the diameter of D_s. If the following condition holds for all $s = 1, 2, \ldots, S$,

$$\left(\sqrt{\frac{\varepsilon_s}{\varepsilon_0}} - 1 \right) \text{diam}(D_s) < \frac{\lambda}{2}, \tag{2.1}$$

then the application of the Born approximation is valid [51]. Then, u_{scat} can be represented as follows:

$$\begin{aligned} u_{\text{scat}}(\mathbf{b}_{m,n}, \mathbf{a}_m) &= k_{\text{b}}^2 \int_D \left(\frac{\varepsilon(\mathbf{r}) - \varepsilon_0}{\varepsilon_0 \mu_0} \right) G(\mathbf{b}_{m,n}, \mathbf{r}) u_{\text{inc}}(\mathbf{r}, \mathbf{a}_m) \mathrm{d}\mathbf{r} \\ &= k_{\text{b}}^2 \int_D \left(\frac{\varepsilon(\mathbf{r}) - \varepsilon_0}{\varepsilon_0 \mu_0} \right) G(\mathbf{b}_{m,n}, \mathbf{r}) G(\mathbf{r}, \mathbf{a}_m) \mathrm{d}\mathbf{r}. \end{aligned} \tag{2.2}$$

Note that if the object is extended, the condition (2.1) is not valid. In this case, peaks of large magnitude appear on the well-illuminated part of the object boundary in the imaging results. We refer to [52] for a detailed discussion and Example 6.1 for a related simulation result.

Remark 2.2 (Conditions of the wavenumber). Since we assume that all D_s are well-separated, that is, there exists a positive constant d such that for all $s, s' = 1, 2, \ldots, S$,

$$\frac{\text{diameter of } D_s}{2} \ll d \quad \text{and} \quad \frac{2.4048}{k} < d \leq |\mathbf{r}_s - \mathbf{r}_{s'}|, \quad s \neq s'.$$

Here, 2.4048 is the first zero of the Bessel function of order zero of the first kind, J_0. Furthermore, if $M, N > 4kR$, good imaging results can be obtained, where R denotes the radius of the circular imaging region (see [53]). Recently, it has been examined that if the antennas are uniformly distributed on a circle and their number is even and greater than eight, good imaging results can be achieved (see [54]).

Based on Remarks 2.1 and 2.2, one can determine the applicable frequency range when a priori information about the objects is available and verify that employing extremely low or high frequencies does not necessarily lead to good imaging results.

3. Indicator function with a single source: design, analysis, and some properties

In this section, we consider the design of an indicator function with a single source. To this end, let $\mathbf{E}(\mathbf{a}_m)$ be the following arrangement of measurement data:

$$\mathbf{E}(\mathbf{a}_m) = \Big(u_{\text{scat}}(\mathbf{b}_{m,1}, \mathbf{a}_m), u_{\text{scat}}(\mathbf{b}_{m,2}, \mathbf{a}_m), \ldots, u_{\text{scat}}(\mathbf{b}_{m,N}, \mathbf{a}_m)\Big). \tag{3.1}$$

Since, by applying the mean-value theorem to (2.2), it is seen that there exists $\mathbf{r}_s \in D_s$, $s = 1, 2, \ldots, S$ such that

$$u_{\text{scat}}(\mathbf{b}_{m,n}, \mathbf{a}_m) = \sum_{s=1}^{S} k_{\text{b}}^2 \,\text{area}(D_s) \left(\frac{\varepsilon_s - \varepsilon_0}{\varepsilon_0 \mu_0}\right) G(\mathbf{b}_{m,n}, \mathbf{r}_s) G(\mathbf{r}_s, \mathbf{a}_m),$$

we can thus examine that

$$\mathbf{E}(\mathbf{a}_m) = \sum_{s=1}^{S} k_{\text{b}}^2 \,\text{area}(D_s) \left(\frac{\varepsilon_s - \varepsilon_0}{\varepsilon_0 \mu_0}\right) G(\mathbf{r}_s, \mathbf{a}_m) \Big(G(\mathbf{b}_{m,1}, \mathbf{r}_s), G(\mathbf{b}_{m,2}, \mathbf{r}_s), \ldots, G(\mathbf{b}_{m,N}, \mathbf{r}_s)\Big).$$

With this, we design the indicator function of the OSM to test the orthogonality relation between $u_{\text{scat}}(\mathbf{b}_{m,n}, \mathbf{a}_m)$ and $G(\mathbf{b}_{m,n}, \cdot)$. To this end, we introduce the following test vector: for each $\mathbf{r}' \in \Omega$,

$$\mathbf{G}(\mathbf{r}') = \Big(G(\mathbf{b}_{m,1}, \mathbf{r}'), G(\mathbf{b}_{m,2}, \mathbf{r}'), \ldots, G(\mathbf{b}_{m,N}, \mathbf{r}')\Big), \tag{3.2}$$

and introduce the corresponding indicator function

$$\mathfrak{F}_{\text{OSM}}(\mathbf{r}', \mathbf{a}_m) = |\mathbf{E}(\mathbf{a}_m) \cdot \overline{\mathbf{G}(\mathbf{r}')}| = \left| \sum_{n=1}^{N} u_{\text{scat}}(\mathbf{b}_{m,n}, \mathbf{r}) \overline{G(\mathbf{b}_{m,n}, \mathbf{r}')} \right|.$$

Then, the map of $\mathfrak{F}_{\text{OSM}}(\mathbf{r}', \mathbf{a}_m)$ will contain large magnitude peaks at $\mathbf{r}' \in D_s$; thus, it will be possible to recognize the existence or outline shape of D_s, $s = 1, 2, \ldots, S$.

Remark 3.1 (Comparison with direct sampling method). The imaging function of the direct sampling method is defined as

$$\mathfrak{F}_{\mathrm{DSM}}(\mathbf{r}', \mathbf{a}_m) = \left| \frac{\mathbf{E}(\mathbf{a}_m)}{\|\mathbf{E}(\mathbf{a}_m)\|} \cdot \frac{\overline{\mathbf{G}(\mathbf{r}')}}{\|\mathbf{G}(\mathbf{r}')\|} \right| = \left| \sum_{n=1}^{N} \frac{u_{\mathrm{scat}}(\mathbf{b}_{m,n}, \mathbf{r}) \overline{G(\mathbf{b}_{m,n}, \mathbf{r}')}}{\|\mathbf{E}(\mathbf{a}_m)\| \|\mathbf{G}(\mathbf{r}')\|} \right|, \tag{3.3}$$

where $\|\mathbf{E}(\mathbf{a}_m)\| = (\mathbf{E}(\mathbf{a}_m) \cdot \overline{\mathbf{E}(\mathbf{a}_m)})^{1/2}$. Hence, we can examine that the orthogonality sampling method has some similarities with the direct sampling method. We refer to [43, 55] for related studies and Example 4.5 for the related simulation result.

To determine the feasibility and some properties of the $\mathfrak{F}_{\mathrm{OSM}}(\mathbf{r}', \mathbf{a}_m)$, we derive the following result.

Theorem 3.1. *Let* $\boldsymbol{\vartheta}_m = (\cos\vartheta_m, \sin\vartheta_m)$, $\boldsymbol{\theta}_{m,n} = (\cos\theta_{m,n}, \sin\theta_{m,n})$, $\boldsymbol{\theta} = (\cos\theta, \sin\theta)$, *and* $\mathbf{r}' - \mathbf{r} = |\mathbf{r}' - \mathbf{r}|(\cos\phi, \sin\phi)$. *Then, for sufficiently large N and f that satisfy the conditions in Remark 2.2,* $\mathfrak{F}_{\mathrm{OSM}}(\mathbf{r}', \mathbf{a}_m)$ *can be represented as follows:*

$$\mathfrak{F}_{\mathrm{OSM}}(\mathbf{r}', \mathbf{a}_m) \approx \left| \frac{N k_{\mathrm{b}}}{8|\mathbf{b}|\pi} \int_D \left(\frac{\varepsilon(\mathbf{r}) - \varepsilon_0}{\varepsilon_0 \mu_0} \right) G(\mathbf{r}, \mathbf{a}_m) \left[J_0(k_{\mathrm{b}}|\mathbf{r}' - \mathbf{r}|) + \frac{3}{\pi} \mathcal{E}(\mathbf{r}', \mathbf{r}, \mathbf{a}_m) \right] \mathrm{d}\mathbf{r} \right|, \tag{3.4}$$

where J_p *denotes the Bessel function of order p and*

$$\mathcal{E}(\mathbf{r}', \mathbf{r}, \mathbf{a}_m) = \sum_{p=1}^{\infty} \frac{(-i)^p}{p} J_p(k_{\mathrm{b}}|\mathbf{r}' - \mathbf{r}|) \cos\left(p(\vartheta_m - \phi)\right) \sin\left(\frac{2p}{3}\pi\right). \tag{3.5}$$

Proof. Since $4k_{\mathrm{b}}|\mathbf{r} - \mathbf{b}_{m,n}| \gg 1$ for $n = 1, 2, \cdots, N$ and

$$|\mathbf{b}_{m,n} - \mathbf{r}| = \sqrt{|\mathbf{b}_{m,n}|^2 - 2\mathbf{b}_{m,n} \cdot \mathbf{r} + |\mathbf{r}|^2} = |\mathbf{b}_{m,n}| - \boldsymbol{\theta}_{m,n} \cdot \mathbf{r} + O\left(\frac{1}{|\mathbf{b}_{m,n}|}\right),$$

the following asymptotic form holds (see [56, Section 9.2] for instance):

$$H_0^{(1)}(k_{\mathrm{b}}|\mathbf{b}_{m,n} - \mathbf{r}|) \approx \sqrt{\frac{2}{\pi k_{\mathrm{b}}|\mathbf{b}_{m,n} - \mathbf{r}|}} e^{i(k_{\mathrm{b}}|\mathbf{b}_{m,n} - \mathbf{r}| - (\pi/4))} \approx \frac{(1-i)}{\sqrt{k_{\mathrm{b}}|\mathbf{b}_{m,n}|\pi}} e^{ik_{\mathrm{b}}(|\mathbf{b}_{m,n}| - \boldsymbol{\theta}_{m,n} \cdot \mathbf{r})}. \tag{3.6}$$

Thus, u_{scat} can be expressed as

$$u_{\mathrm{scat}}(\mathbf{b}_{m,n}, \mathbf{a}_m) \approx -\frac{k_{\mathrm{b}}^2(1+i)e^{ik_{\mathrm{b}}|\mathbf{b}_{m,n}|}}{4\sqrt{k_{\mathrm{b}}|\mathbf{b}_{m,n}|\pi}} \int_D \left(\frac{\varepsilon(\mathbf{r}) - \varepsilon_0}{\varepsilon_0 \mu_0} \right) G(\mathbf{r}, \mathbf{a}_m) e^{-ik_{\mathrm{b}}\boldsymbol{\theta}_{m,n} \cdot \mathbf{r}} \mathrm{d}\mathbf{r},$$

from which we can evaluate

$$\begin{aligned}
&\sum_{n=1}^{N} u_{\mathrm{scat}}(\mathbf{b}_{m,n}, \mathbf{a}_m) \overline{G(\mathbf{b}_{m,n}, \mathbf{r}')} \\
&\approx -\sum_{n=1}^{N} \left(\frac{k_{\mathrm{b}}^2(1+i)e^{ik_{\mathrm{b}}|\mathbf{b}_{m,n}|}}{4\sqrt{k_{\mathrm{b}}|\mathbf{b}_{m,n}|\pi}} \int_D \left(\frac{\varepsilon(\mathbf{r}) - \varepsilon_0}{\varepsilon_0 \mu_0} \right) G(\mathbf{r}, \mathbf{a}_m) e^{-ik_{\mathrm{b}}\boldsymbol{\theta}_{m,n} \cdot \mathbf{r}} \mathrm{d}\mathbf{r} \right) \frac{(-1+i)e^{-ik_{\mathrm{b}}|\mathbf{b}_{m,n}|}}{4\sqrt{k_{\mathrm{b}}|\mathbf{b}_{m,n}|\pi}} e^{ik_{\mathrm{b}}\boldsymbol{\theta}_{m,n} \cdot \mathbf{r}'} \\
&= \frac{k_{\mathrm{b}}}{8|\mathbf{b}|\pi} \int_D \left(\frac{\varepsilon(\mathbf{r}) - \varepsilon_0}{\varepsilon_0 \mu_0} \right) G(\mathbf{r}, \mathbf{a}_m) \left(\sum_{n=1}^{N} e^{ik_{\mathrm{b}}\boldsymbol{\theta}_{m,n} \cdot (\mathbf{r}' - \mathbf{r})} \right) \mathrm{d}\mathbf{r}.
\end{aligned}$$

Since the following relation holds uniformly (see [57] for derivation):

$$\frac{1}{\beta-\alpha}\int_{\alpha}^{\beta} e^{ix\cos(\theta-\phi)}\mathrm{d}\theta = J_0(x) + \frac{4}{\beta-\alpha}\sum_{p=1}^{\infty}\frac{i^p}{p}J_p(x)\cos\frac{p(\beta+\alpha-2\phi)}{2}\sin\frac{p(\beta-\alpha)}{2}, \tag{3.7}$$

by letting $\boldsymbol{\theta}\cdot(\mathbf{r}'-\mathbf{r}) = |\mathbf{r}'-\mathbf{r}|\cos(\theta-\phi)$ and $\triangle\theta = (\theta_{m,N}-\theta_{m,1})/N = 4\pi/3N$, we can derive

$$\begin{aligned}\sum_{n=1}^{N} e^{ik_{\mathrm{b}}\boldsymbol{\theta}_{m,n}\cdot(\mathbf{r}'-\mathbf{r})} &= \frac{N}{N\triangle\theta}\sum_{n=1}^{N} e^{ik_{\mathrm{b}}\boldsymbol{\theta}_{m,n}\cdot(\mathbf{r}'-\mathbf{r})}\triangle\theta \approx \frac{3N}{4\pi}\int_{\mathbb{S}_m^1} e^{ik_{\mathrm{b}}\boldsymbol{\theta}\cdot(\mathbf{r}'-\mathbf{r})}\mathrm{d}\boldsymbol{\theta} = \frac{3N}{4\pi}\int_{\vartheta_m+\pi/6}^{\vartheta_m+5\pi/6} e^{ik_{\mathrm{b}}|\mathbf{r}'-\mathbf{r}|\cos(\theta-\phi)}\mathrm{d}\theta \\ &\approx N\left[J_0(k_{\mathrm{b}}|\mathbf{r}'-\mathbf{r}|) + \frac{3}{\pi}\sum_{p=1}^{\infty}\frac{(-i)^p}{p}J_p(k_{\mathrm{b}}|\mathbf{r}'-\mathbf{r}|)\cos\left(p(\vartheta_m-\phi)\right)\sin\left(\frac{2p}{3}\pi\right)\right].\end{aligned}$$

Hence,

$$\sum_{n=1}^{N} u_{\mathrm{scat}}(\mathbf{b}_{m,n},\mathbf{a}_m)\overline{G(\mathbf{b}_{m,n},\mathbf{r}')} \approx \frac{Nk_{\mathrm{b}}}{8|\mathbf{b}|\pi}\int_D\left(\frac{\varepsilon(\mathbf{r})-\varepsilon_0}{\varepsilon_0\mu_0}\right)G(\mathbf{r},\mathbf{a}_m)\left[J_0(k_{\mathrm{b}}|\mathbf{r}'-\mathbf{r}|) + \frac{3}{\pi}\mathcal{E}(\mathbf{r}',\mathbf{r},\mathbf{a}_m)\right]\mathrm{d}\mathbf{r}$$

and (3.4) can be obtained. □

Based on Theorem 3.1, we can examine some properties of the indicator function.

Remark 3.2 (Availability and limitation of object detection). Since $J_0(0) = 1$ and $J_p(0) = 0$ for $p = 1, 2, \ldots$, we can examine that $J_0(k_{\mathrm{b}}|\mathbf{r}'-\mathbf{r}|) = 1$ and $\mathcal{E}(\mathbf{r}',\mathbf{r},\mathbf{a}_m) = 0$ when $\mathbf{r}' = \mathbf{r} \in D$. Thus, $\mathfrak{F}_{\mathrm{OSM}}(\mathbf{r}',\mathbf{a}_m)$ is expected to exhibit peaks of magnitudes $\frac{Nk_{\mathrm{b}}}{8|\mathbf{b}|\pi}\left(\frac{\varepsilon_s-\varepsilon_0}{\varepsilon_0\mu_0}\right)|G(\mathbf{r}',\mathbf{a}_m)|\,\mathrm{area}(D_s)$ at the $\mathbf{r}' \in D_s$ sought. This means that the imaging performance of the $\mathfrak{F}_{\mathrm{OSM}}(\mathbf{r}',\mathbf{a}_m)$ will be strongly dependent on the position of the emitter $\mathcal{A}_m$ because $\mathfrak{F}_{\mathrm{OSM}}(\mathbf{r}_s,\mathbf{a}_m) \propto |G(\mathbf{r}_s,\mathbf{a}_m)|$. Moreover, if one applies an extremely high frequency, then the value of $|G(\mathbf{r},\mathbf{a}_m)J_0(k_{\mathrm{b}}|\mathbf{r}'-\mathbf{r}|)|$ will be negligible because $|J_0(k_{\mathrm{b}}|\mathbf{r}'-\mathbf{r}|)| \le 1$ and

$$|G(\mathbf{r},\mathbf{a}_m)| = \left|\frac{(1-i)e^{ik_{\mathrm{b}}|\mathbf{b}_{m,n}|}}{\sqrt{k_{\mathrm{b}}|\mathbf{b}_{m,n}|\pi}}e^{-ik_{\mathrm{b}}\boldsymbol{\theta}_{m,n}\cdot\mathbf{r}_s}\right| \longrightarrow 0 \quad \text{as} \quad f \longrightarrow \infty.$$

Thus, the effect of $J_0(k_{\mathrm{b}}|\mathbf{r}'-\mathbf{r}|)$ becomes negligible so that it will be unable to distinguish between unknown objects and several artifacts in the map of $\mathfrak{F}_{\mathrm{OSM}}(\mathbf{r}',\mathbf{a}_m)$. This means that the application of an extremely high frequency does not guarantee the detection of an unknown object.

Remark 3.3 (Detection of multiple objects). Here, we assume that there exist two objects, D_1 and D_2, located at $\mathbf{r}_1$ and $\mathbf{r}_2$, respectively. Then, the following relation must be satisfied to distinguish the objects through the map of $\mathfrak{F}_{\mathrm{OSM}}(\mathbf{r}',\mathbf{a}_m)$:

$$|\mathbf{r}_1-\mathbf{r}_2| > \frac{2.4048}{k}. \tag{3.8}$$

In Section 4, the scattered field data were generated in the presence of two circular dielectric objects centered at $\mathbf{r}_1 = 0.045\,\mathrm{m}$ and $\mathbf{r}_2 = -0.045\,\mathrm{m}$, i.e., $|\mathbf{r}_1-\mathbf{r}_2| = 0.09\,\mathrm{m}$. If $f = 1\,\mathrm{GHz}$, then $2.4048/k = 0.1147\,\mathrm{m}$ because $k = 20.9585$. As a result, the two objects cannot be distinguished through the map of $\mathfrak{F}_{\mathrm{OSM}}(\mathbf{r}',\mathbf{a}_m)$ because k does not satisfy the relation (3.8). If $f \ge 2\,\mathrm{GHz}$, then D_1 and D_2 can be distinguished because k satisfies the relation (3.8). Thus, the application of a low frequency does not guarantee the detection of unknown objects using the OSM with a single source.

Remark 3.4 (Effect of the factor $\mathcal{E}(\mathbf{r}', \mathbf{r}, \mathbf{a}_m)$). Owing to (3.5), the factor $\mathcal{E}(\mathbf{r}', \mathbf{r}, \mathbf{a}_m)$ does not contribute to the identification of objects because $\mathcal{E}(\mathbf{r}', \mathbf{r}, \mathbf{a}_m) = 0$ when $\mathbf{r}' = \mathbf{r} \in D$ on the basis of the fact that $J_p(0) = 0$ for $p = 1, 2, \ldots$, and it disturbs the identification process by generating several artifacts due to the oscillating property of J_p. To examine the influence of $\mathcal{E}(\mathbf{r}', \mathbf{r}, \mathbf{a}_m)$, we consider the following quantity:

$$\mathcal{D}_1(x) = \left| J_0(k_b|x|) + \frac{3}{\pi} \sum_{p=1}^{10^6} \frac{(-i)^p}{p} J_p(k_b|x|) \sin\left(\frac{2p}{3}\pi\right) \right|.$$

This is a one-dimensional version of $|J_0(k_b|\mathbf{r} - \mathbf{r}'|) + \frac{3}{\pi}\mathcal{E}(\mathbf{r}', \mathbf{r}, \mathbf{a}_m)|$ for $\mathbf{a}_m = (1, 0)$, i.e., $\vartheta_m = 0$ and $\mathbf{r} = (0, 0)$. Since $|J_0(k_b|x|)| \leq \mathcal{D}_1(x)$, and by comparing the oscillatory properties of $J_0(k_b|x|)$ and $\mathcal{D}_1(x)$, we can say that the maps of $\mathfrak{F}_{\mathrm{OSM}}(\mathbf{r}', \mathbf{a}_m)$ will contain several artifacts with large magnitudes, which will disturb the recognition of the existence of objects. We refer to Figure 2.

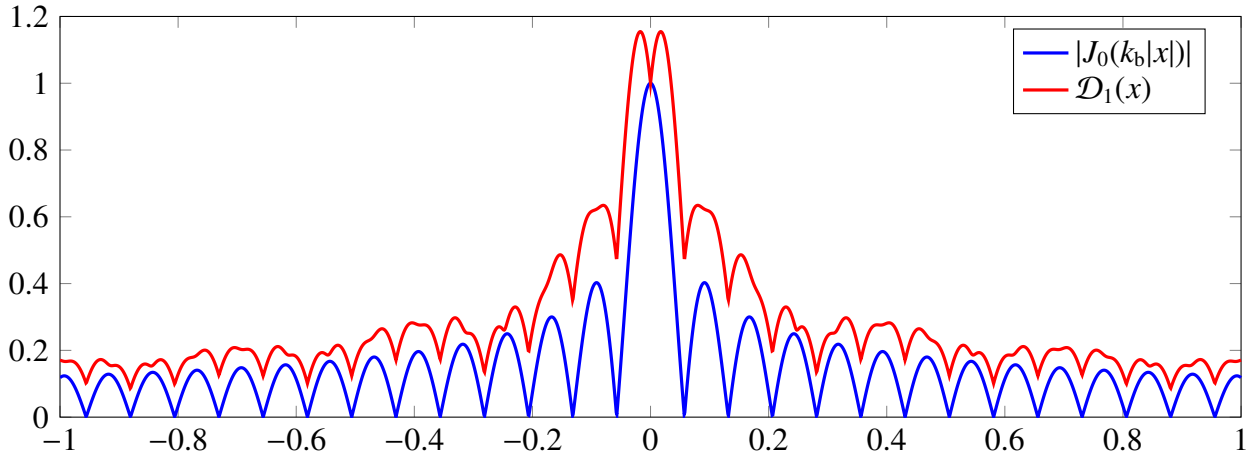

Figure 2. Plots of $|J_0(k_b|x|)|$ and $\mathcal{D}_1(x)$ for $-1 \leq x \leq 1$ and $f = 2\,\mathrm{GHz}$.

4. Simulation results with synthetic and Fresnel experimental database

Here, we present simulation results obtained using synthetic and Fresnel experimental database [46]. Here, the emitters and receivers were placed on circles centered at the origin with radii $|\mathbf{a}_m| = 0.72\,\mathrm{m}$ and $|\mathbf{b}_{m,n}| = 0.76\,\mathrm{m}$, respectively, and the imaging region Ω was selected as a square $(-0.1\,\mathrm{m}, 0.1\,\mathrm{m}) \times (-0.1\,\mathrm{m}, 0.1\,\mathrm{m})$ to satisfy the relation $4k_b|\mathbf{r} - \mathbf{a}_m|, 4k_b|\mathbf{r} - \mathbf{b}_{m,n}| \gg 1$ for $m = 1, 2, \ldots, M(= 36)$ and $n = 1, 2, \ldots, N(= 49)$. In addition, the range of the receivers was restricted from 60° to 300°, with a step size of $\triangle\theta = 5°$ based on the location of each emitter (see Figure 1 for an illustration).

For the simulation results with synthetic data, we selected circular objects comprised of three filled dielectric cylinders D_s, $s = 1, 2, 3$ with a circular cross section of radius $r_1 = 0.015\,\mathrm{m}$, $r_2 = 0.020\,\mathrm{m}$, and $r_3 = 0.010\,\mathrm{m}$ and permittivity $\varepsilon_1 = 4\varepsilon_0$, $\varepsilon_2 = 5\varepsilon_0$, and $\varepsilon_3 = 5\varepsilon_0$ centered at $\mathbf{r}_1 = (0.000\,\mathrm{m}, 0.045\,\mathrm{m})$, $\mathbf{r}_2 = (0.060\,\mathrm{m}, -0.045\,\mathrm{m})$, and $\mathbf{r}_3 = (-0.060\,\mathrm{m}, -0.045\,\mathrm{m})$. With this setting, the measurement data were generated by using the Feldberechnung für Körper mit beliebiger Oberfläche (FEKO).

For the simulation results with Fresnel database, we selected objects comprised of two filled dielectric cylinders D_1 and D_2 with a circular cross section of radius 0.015 m and permittivity $\varepsilon_s = (3 \pm 0.3)\varepsilon_0$

centered at $\mathbf{r}_1 = (0.045\,\text{m}, 0.010\,\text{m})$ and $\mathbf{r}_2 = (-0.045\,\text{m}, 0)$, respectively*.

With this setting, we generated the imaging results of $\mathfrak{F}_{\text{OSM}}(\mathbf{r}', \mathbf{a}_m)$ with $m = 1$, 10, and 25. Refer to Figure 3 for antenna arrangements. On average, all the numerical experiments were completed within 1.38 seconds.

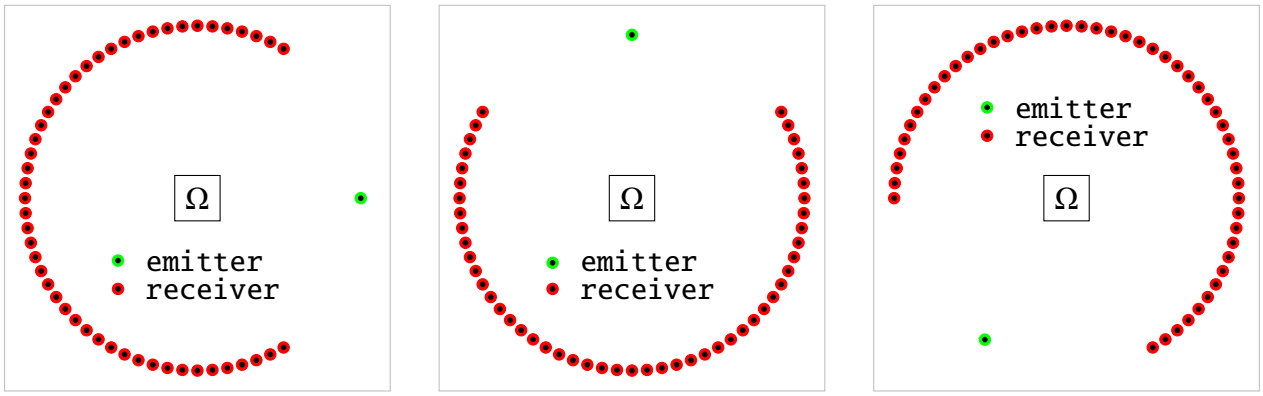

(a) Receiver arrangement for $\mathcal{A}_1$ (b) Receiver arrangement for $\mathcal{A}_{10}$ (c) Receiver arrangement for $\mathcal{A}_{25}$

Figure 3. Illustration of the antenna arrangement corresponding to emitters $\mathcal{A}_1$, $\mathcal{A}_{10}$, and $\mathcal{A}_{25}$, as well as the imaging region Ω.

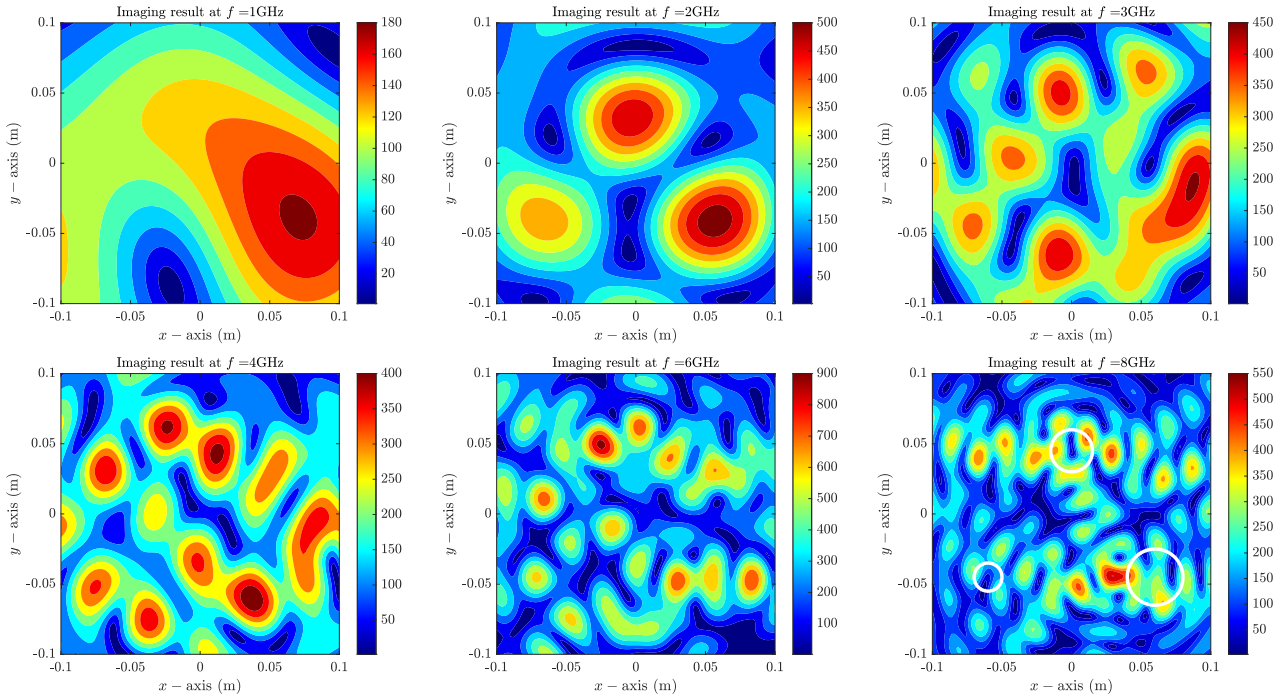

Figure 4. (Example 4.1) Maps of $\mathfrak{F}_{\text{OSM}}(\mathbf{r}', \mathbf{a}_1)$. White circles describe ∂D_s.

*In the literature [46], $\mathbf{r}_1 = (0.045\,\text{m}, 0)$ was given; however, in several previous results [23, 27, 58, 59], the accurate location of D_1 appeared to be $\mathbf{r}_1 = (0.045\,\text{m}, 0.010\,\text{m})$.

Example 4.1 (Imaging results with synthetic data for $\mathbf{a}_1$). Figure 4 shows the maps of $\mathfrak{F}_{\mathrm{OSM}}(\mathbf{r}', \mathbf{a}_1)$ with $\mathbf{a}_1 = 0.72\,\mathrm{m}(\cos 0°, \sin 0°)$ at several frequencies. Following the imaging results, it seems be possible to recognize the existence of three objects, but their exact locations and shapes cannot be identified when $f = 2\,\mathrm{GHz}$. Moreover, it is impossible to recognize the existence of the objects when $f = 1, 3, 4, 6, 8\,\mathrm{GHz}$.

Example 4.2 (Imaging results with synthetic data for $\mathbf{a}_{10}$). Figure 5 shows the maps of $\mathfrak{F}_{\mathrm{OSM}}(\mathbf{r}', \mathbf{a}_{10})$ with $\mathbf{a}_{10} = 0.72\,\mathrm{m}(\cos 90°, \sin 90°)$ at several frequencies. In contrast to the results shown in Figure 4, it is possible to recognize the existence of the three objects when $f = 2, 3\,\mathrm{GHz}$, but their accurate locations and outline shapes cannot be retrieved. Similar to the results shown in Figure 4, it remains impossible to recognize them when $f = 1\,\mathrm{GHz}$ and $f \geq 4\,\mathrm{GHz}$.

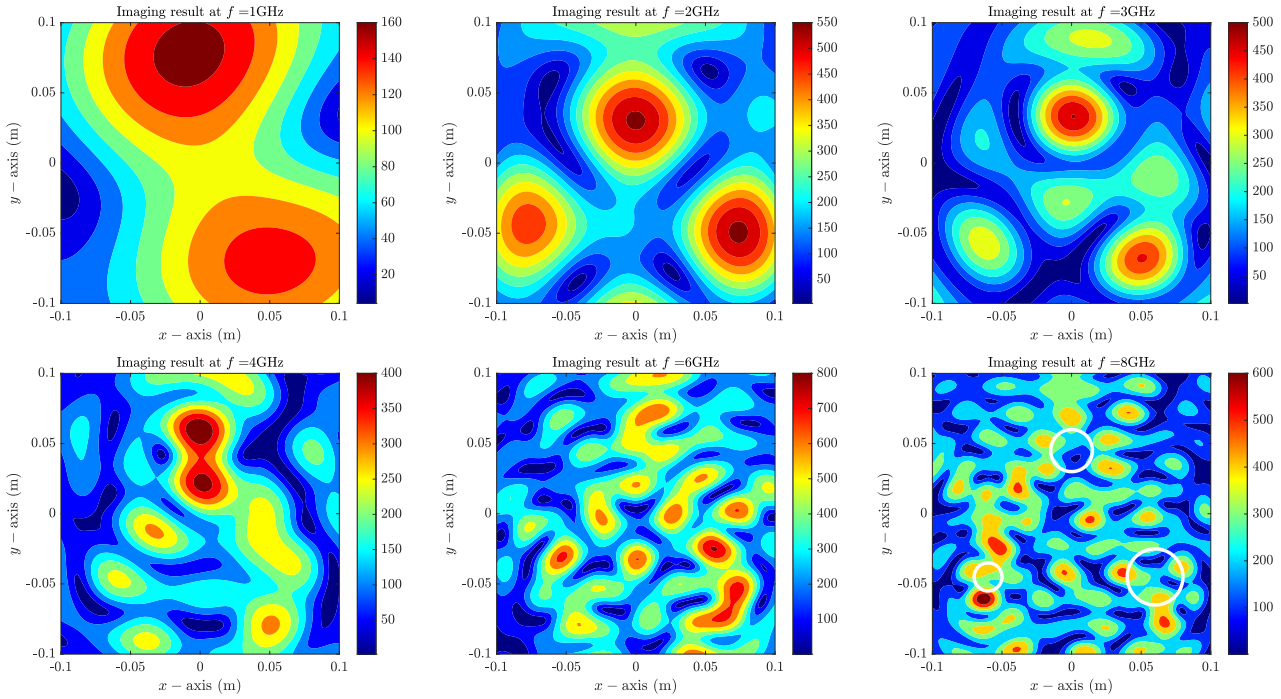

Figure 5. (Example 4.2) Maps of $\mathfrak{F}_{\mathrm{OSM}}(\mathbf{r}', \mathbf{a}_{10})$. White circles describe ∂D_s.

Example 4.3 (Imaging results with synthetic data for $\mathbf{a}_{25}$). Figure 6 shows the maps of $\mathfrak{F}_{\mathrm{OSM}}(\mathbf{r}', \mathbf{a}_{25})$ with $\mathbf{a}_{25} = 0.72\,\mathrm{m}(\cos 240°, \sin 240°)$ at several frequencies. Similar to the results presented in Figure 4, the existence of the three objects can be recognized when $f = 2\,\mathrm{GHz}$, but their locations and outline shapes cannot be retrieved. Nonetheless, it is still impossible to recognize the objects when $f = 1\,\mathrm{GHz}$ and $f \geq 3\,\mathrm{GHz}$.

Example 4.4 (Imaging results with Fresnel database for $\mathbf{a}_1$). Figure 7 shows the maps of $\mathfrak{F}_{\mathrm{OSM}}(\mathbf{r}', \mathbf{a}_1)$ with $\mathbf{a}_1 = 0.72\,\mathrm{m}(\cos 0°, \sin 0°)$ at several frequencies. Based on the simulation results, it is impossible to recognize the objects through the map of $\mathfrak{F}_{\mathrm{OSM}}(\mathbf{r}', \mathbf{a}_1)$ when $f \leq 2\,\mathrm{GHz}$ and $f \geq 6\,\mathrm{GHz}$. Fortunately, peaks of large magnitudes appear at $\mathbf{r}_1$ and $\mathbf{r}_2$; thus, we can recognize the existence of the two objects. However, their outline shape cannot be determined.

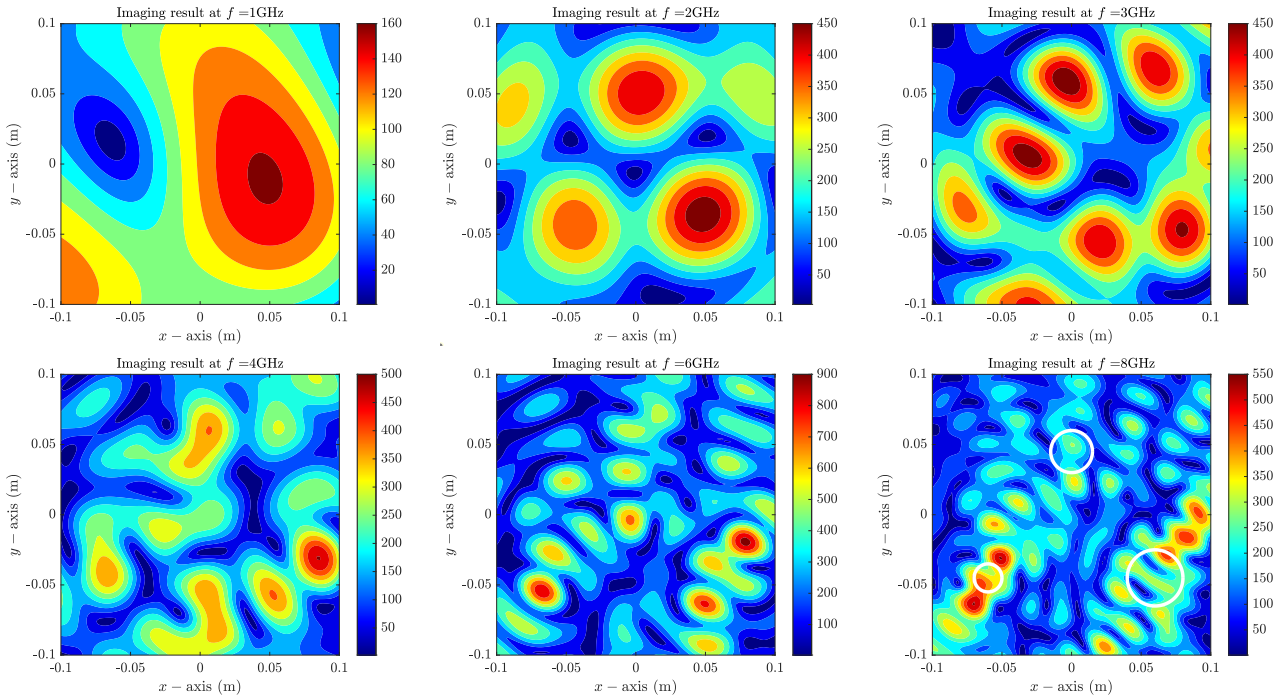

Figure 6. (Example 4.3) Maps of $\mathfrak{F}_{\mathrm{OSM}}(\mathbf{r}', \mathbf{a}_{25})$. White circles describe ∂D_s.

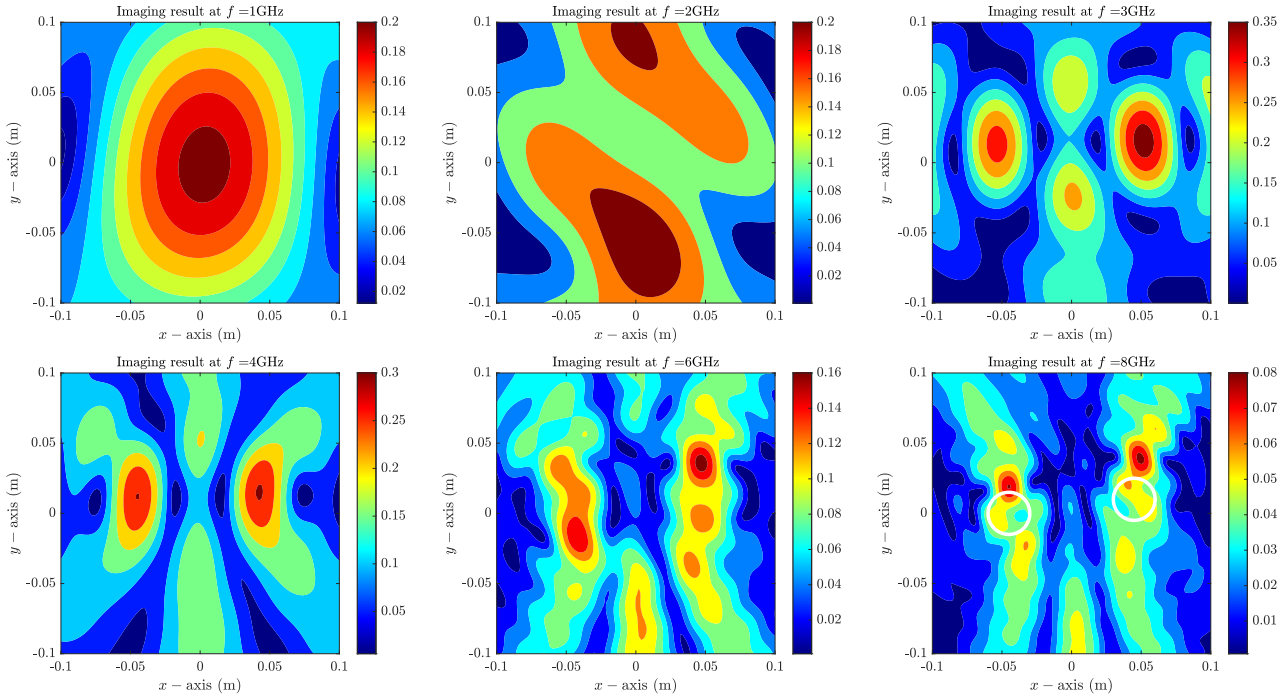

Figure 7. (Example 4.4) Maps of $\mathfrak{F}_{\mathrm{OSM}}(\mathbf{r}', \mathbf{a}_{1})$. White circles describe ∂D_s.

Figure 8 shows the maps of $\mathfrak{F}_{\mathrm{OSM}}(\mathbf{r}', \mathbf{a}_1)$ at several frequencies when the measured scattered-field data were contaminated with 15 dB white Gaussian random noise. Compared with the results in

Figure 7, the imaging results appear very similar, indicating that the OSM with single source is robust to random noise.

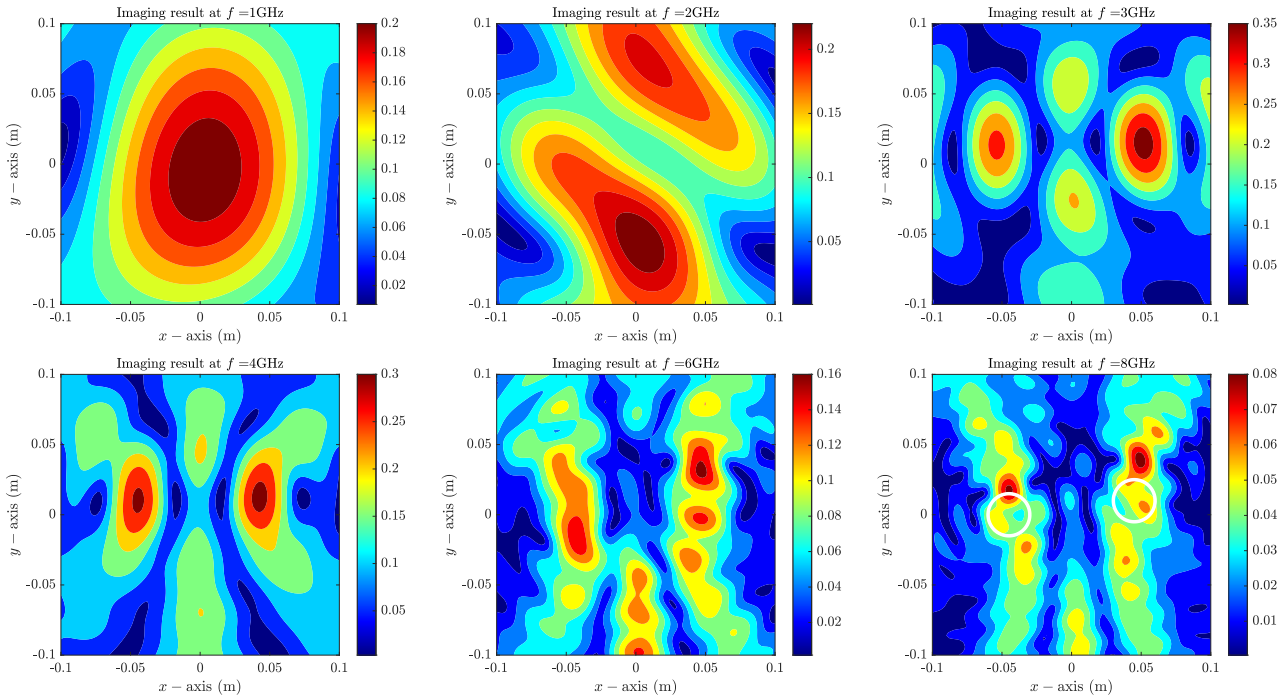

Figure 8. (Example 4.4) Maps of $\mathfrak{F}_{\mathrm{OSM}}(\mathbf{r}', \mathbf{a}_1)$ with noisy data. White circles describe ∂D_s.

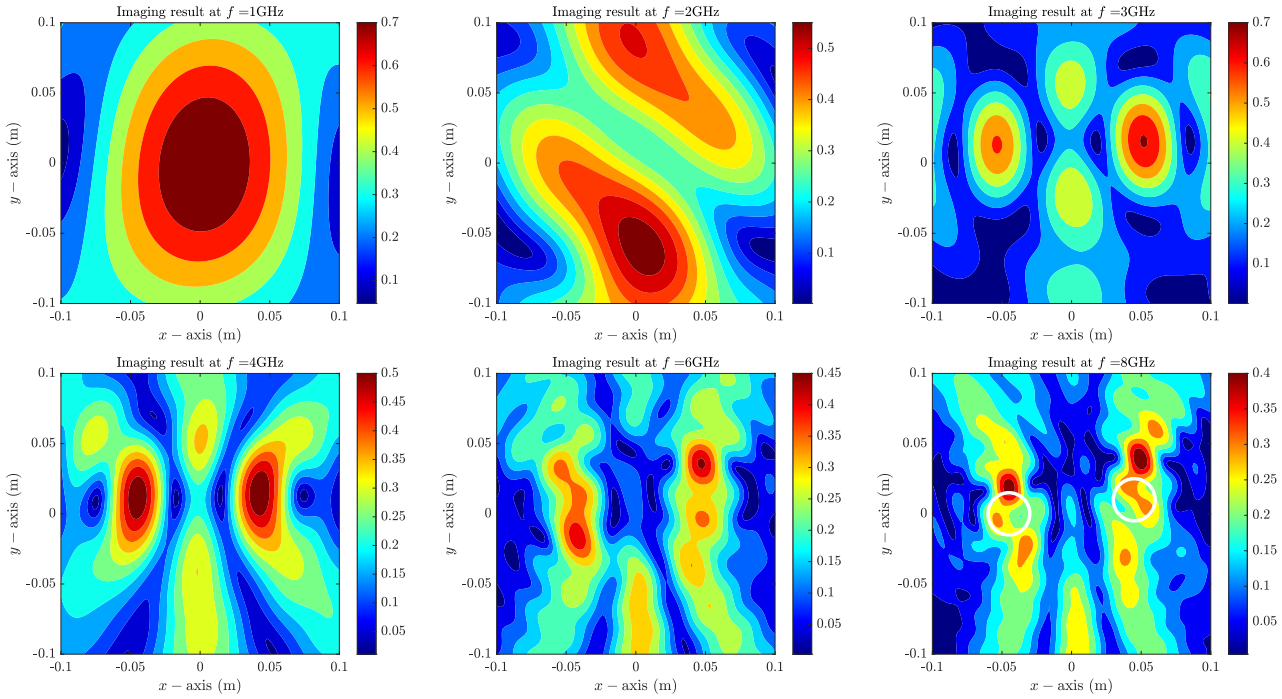

Figure 9. (Example 4.5) Maps of $\mathfrak{F}_{\mathrm{DSM}}(\mathbf{r}', \mathbf{a}_1)$. White circles describe ∂D_s.

Example 4.5 (Comparison with direct sampling method). Here, we consider the imaging results obtained using the direct sampling method. Figure 9 presents the maps of $\mathfrak{F}_{\mathrm{DSM}}(\mathbf{r}', \mathbf{a}_1)$ defined in (3.3) at several frequencies. Compared with the imaging results in Figure 7, they appear almost identical, except for slight differences in the residual artifacts and the values of $\mathfrak{F}_{\mathrm{OSM}}(\mathbf{r}', \mathbf{a}_1)$ and $\mathfrak{F}_{\mathrm{DSM}}(\mathbf{r}', \mathbf{a}_1)$.

Example 4.6 (Imaging results with Fresnel database for $\mathbf{a}_{10}$). Figure 10 shows the maps of $\mathfrak{F}_{\mathrm{OSM}}(\mathbf{r}', \mathbf{a}_{10})$ with $\mathbf{a}_{10} = 0.72\,\mathrm{m}(\cos 90°, \sin 90°)$ at several frequencies. In contrast to the results shown in Figure 7, here, it is possible to recognize the existence of the two objects at $f = 2\,\mathrm{GHz}$; however, it remains impossible to recognize them when $f = 1\,\mathrm{GHz}$ and $f \geq 6\,\mathrm{GHz}$. In addition, it appears to be difficult to recognize the existence of the objects when $f = 4\,\mathrm{GHz}$ due to the appearance of two artifacts with large magnitudes.

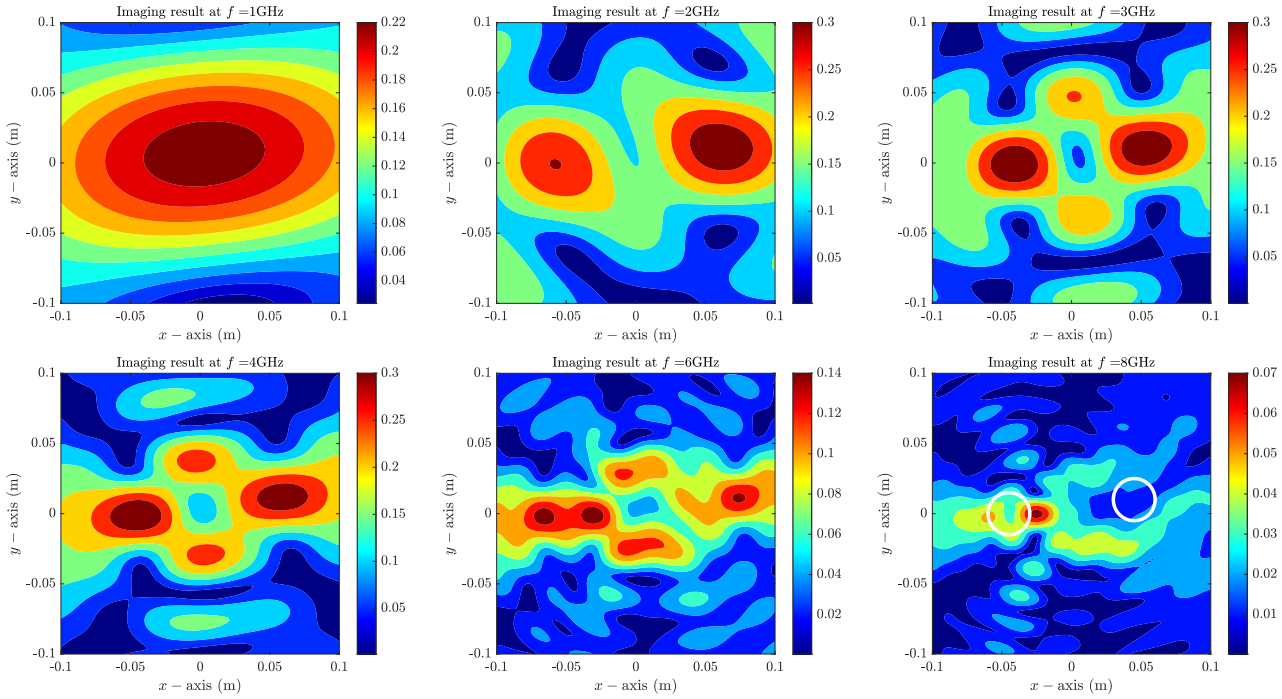

Figure 10. (Example 4.6) Maps of $\mathfrak{F}_{\mathrm{OSM}}(\mathbf{r}', \mathbf{a}_{10})$. White circles describe ∂D_s.

Example 4.7 (Imaging results with Fresnel database for $\mathbf{a}_{25}$). Figure 11 shows the maps of $\mathfrak{F}_{\mathrm{OSM}}(\mathbf{r}', \mathbf{a}_{25})$ with $\mathbf{a}_{25} = 0.72\,\mathrm{m}(\cos 240°, \sin 240°)$ at several frequencies. In contrast to the results presented in Figures 7 and 10, the existence of the two objects can be recognized when $f = 2\,\mathrm{GHz}$, and a large-magnitude peak only appeares when $\mathbf{r}' \in D_1$ and when $f = 3, 4\,\mathrm{GHz}$. Nonetheless, it is still impossible to recognize the objects when $f = 1\,\mathrm{GHz}$ and $f \geq 6\,\mathrm{GHz}$.

According to the simulation results with synthetic and Fresenel experimental database, as well as Remarks 3.2 and 3.3, we conclude that the imaging performance of the OSM with a single source is strongly dependent on the operated frequency and the location of the emitter. Thus, designing another indicator function for the OSM is necessary to improve the imaging performance.

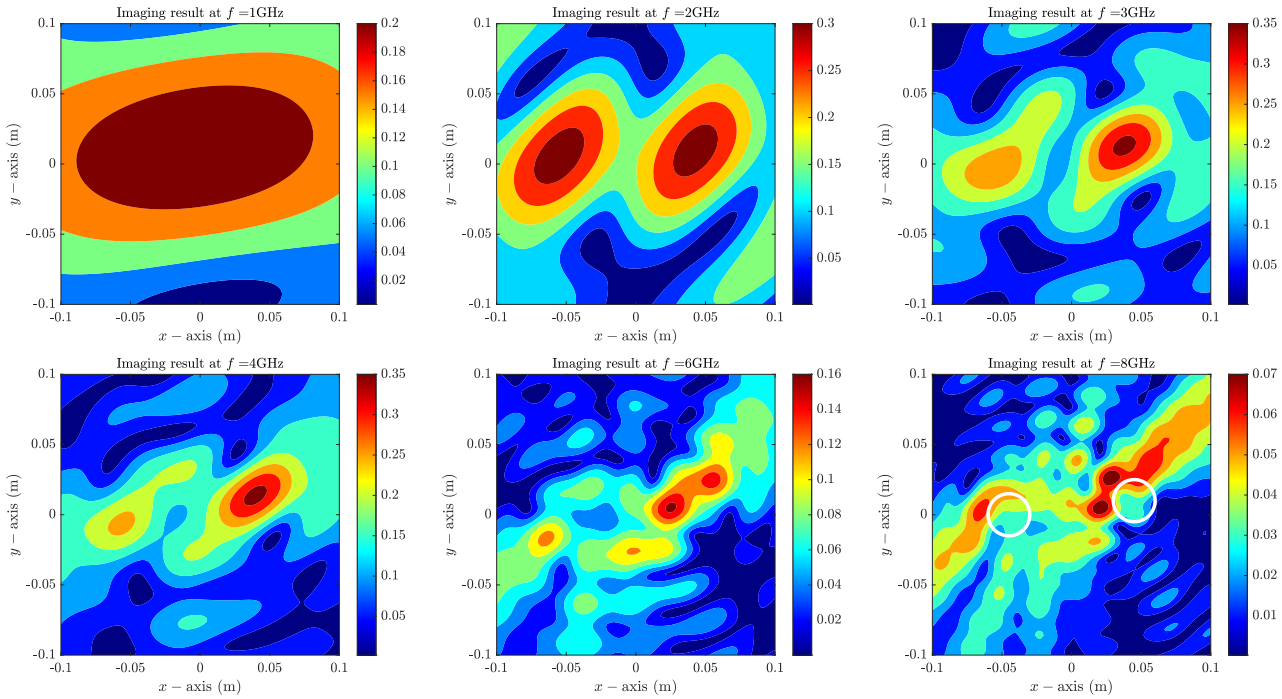

Figure 11. (Example 4.7) Maps of $\mathfrak{F}_{\mathrm{OSM}}(\mathbf{r}', \mathbf{a}_{25})$. White circles describe ∂D_s.

5. Indicator function with multiple sources: design, analysis, and some properties

Following several previous studies [57, 60, 61], it has been confirmed that the application of multiple sources and/or frequencies improves the imaging performance. Following the literatures [40, 44], we can examine several simulation results for the improvement of the multi-frequency OSM. Here, we consider the single-frequency OSM with multiple sources for a proper identification of objects. In addition, in reference to another study [40], the following indicator function with multiple sources can be used: for each $\mathbf{r}' \in \Omega$,

$$\mathfrak{F}_{\mathrm{OSMM}}(\mathbf{r}') = \sum_{m=1}^{M} \mathfrak{F}_{\mathrm{OSM}}(\mathbf{r}', \mathbf{a}_m).$$

Although we can obtain a good result using the map of $\mathfrak{F}_{\mathrm{OSMM}}(\mathbf{r}')$, we introduce a new indicator function to obtain a better result (see [62, 63] also). To this end, we denote $\mathbf{F}(\mathbf{r}')$ as the following arrangement:

$$\mathbf{F}(\mathbf{r}') = \Big(\Phi(\mathbf{r}', \mathbf{a}_1), \Phi(\mathbf{r}', \mathbf{a}_2), \ldots, \Phi(\mathbf{r}', \mathbf{a}_N)\Big)$$

$$= \frac{Nk_{\mathrm{b}}}{8|\mathbf{b}|\pi} \begin{pmatrix} \displaystyle\int_D \left(\frac{\varepsilon(\mathbf{r})-\varepsilon_0}{\varepsilon_0\mu_0}\right) G(\mathbf{r},\mathbf{a}_1)\Big[J_0(k|\mathbf{r}'-\mathbf{r}|)+\frac{3}{\pi}\mathcal{E}(\mathbf{r}',\mathbf{r},\mathbf{a}_1)\Big]\mathrm{d}\mathbf{r} \\ \displaystyle\int_D \left(\frac{\varepsilon(\mathbf{r})-\varepsilon_0}{\varepsilon_0\mu_0}\right) G(\mathbf{r},\mathbf{a}_2)\Big[J_0(k|\mathbf{r}'-\mathbf{r}|)+\frac{3}{\pi}\mathcal{E}(\mathbf{r}',\mathbf{r},\mathbf{a}_2)\Big]\mathrm{d}\mathbf{r} \\ \vdots \\ \displaystyle\int_D \left(\frac{\varepsilon(\mathbf{r})-\varepsilon_0}{\varepsilon_0\mu_0}\right) G(\mathbf{r},\mathbf{a}_m)\Big[J_0(k|\mathbf{r}'-\mathbf{r}|)+\frac{3}{\pi}\mathcal{E}(\mathbf{r}',\mathbf{r},\mathbf{a}_m)\Big]\mathrm{d}\mathbf{r} \end{pmatrix}^T,$$

where $\Phi(\mathbf{r}',\mathbf{a}_m)$ satisfies $\mathfrak{F}_{\mathrm{OSM}}(\mathbf{r}',\mathbf{a}_m) = |\Phi(\mathbf{r}',\mathbf{a}_m)|$. Then, based on the structure of the $\mathbf{F}(\mathbf{r}')$, it appears natural to test the orthogonality relation between $\Phi(\mathbf{r}',\mathbf{a}_m)$ and $G(\cdot,\mathbf{a}_m)$. Thus, by introducing a test vector

$$\mathbf{H}(\mathbf{r}') = \Big(G(\mathbf{r}',\mathbf{a}_1), G(\mathbf{r}',\mathbf{a}_2), \ldots, G(\mathbf{r}',\mathbf{a}_M)\Big), \quad \mathbf{r}' \in \Omega,$$

the following indicator function with multiple sources can be introduced:

$$\mathfrak{F}_{\mathrm{MOSM}}(\mathbf{r}') = |\mathbf{F}(\mathbf{r}')\cdot\overline{\mathbf{H}(\mathbf{r}')}| = \left|\sum_{m=1}^{M}\Phi(\mathbf{r}',\mathbf{a}_m)\overline{G(\mathbf{r}',\mathbf{a}_m)}\right|.$$

Then, the map of $\mathfrak{F}_{\mathrm{MOSM}}(\mathbf{r}')$ will contain large-magnitude peaks at $\mathbf{r}' \in D_s$; thus, it will be possible to recognize the existence or outline shape of D_s, $s = 1, 2, \ldots, S$. Here, to discover the feasibility and some properties of the $\mathfrak{F}_{\mathrm{MOSM}}(\mathbf{r}')$, we derive the following.

Theorem 5.1. *Let $\boldsymbol{\vartheta} = (\cos\vartheta, \sin\vartheta)$, $\boldsymbol{\vartheta}_m = (\cos\vartheta_m, \sin\vartheta_m)$, and $\mathbf{r}' - \mathbf{r} = |\mathbf{r}' - \mathbf{r}|(\cos\phi, \sin\phi)$. Then, for sufficiently large M, N, and f that satisfy the conditions in Remark 2.2, $\mathfrak{F}_{\mathrm{MOSM}}(\mathbf{r}')$ can be represented as follows:*

$$\mathfrak{F}_{\mathrm{MOSM}}(\mathbf{r}') \approx \left|\frac{MN}{4|\mathbf{a}||\mathbf{b}|\pi^2}\int_D \left(\frac{\varepsilon(\mathbf{r})-\varepsilon_0}{\varepsilon_0\mu_0}\right)\left(J_0(k_{\mathrm{b}}|\mathbf{r}'-\mathbf{r}|)^2+\frac{3}{\pi}\mathcal{M}(\mathbf{r}',\mathbf{r})\right)\mathrm{d}\mathbf{r}\right|, \tag{5.1}$$

where

$$\mathcal{M}(\mathbf{r}',\mathbf{r}) = \sum_{p=1}^{\infty}\frac{i^p}{p}J_p(k_{\mathrm{b}}|\mathbf{r}'-\mathbf{r}|)^2\sin\left(\frac{2p}{3}\pi\right).$$

Proof. Following (3.4), we obtain the following:

$$\begin{aligned}
&\sum_{m=1}^{M}\Phi(\mathbf{r}',\mathbf{a}_m)\overline{G(\mathbf{r}',\mathbf{a}_m)} \\
&\approx \sum_{m=1}^{M}\left[\frac{Nk_{\mathrm{b}}}{8|\mathbf{b}|\pi}\int_D\left(\frac{\varepsilon(\mathbf{r})-\varepsilon_0}{\varepsilon_0\mu_0}\right)G(\mathbf{r},\mathbf{a}_m)\left(J_0(k_{\mathrm{b}}|\mathbf{r}'-\mathbf{r}|)+\frac{3}{\pi}\mathcal{E}(\mathbf{r}',\mathbf{r},\mathbf{a}_m)\right)\mathrm{d}\mathbf{r}\right]\overline{G(\mathbf{r}',\mathbf{a}_m)} \\
&= \frac{Nk_{\mathrm{b}}}{8|\mathbf{b}|\pi}\int_D\left(\frac{\varepsilon(\mathbf{r})-\varepsilon_0}{\varepsilon_0\mu_0}\right)\sum_{m=1}^{M}\left[G(\mathbf{r},\mathbf{a}_m)\overline{G(\mathbf{r}',\mathbf{a}_m)}\left(J_0(k_{\mathrm{b}}|\mathbf{r}'-\mathbf{r}|)+\frac{3}{\pi}\mathcal{E}(\mathbf{r}',\mathbf{r},\mathbf{a}_m)\right)\right]\mathrm{d}\mathbf{r}.
\end{aligned}$$

Since M is sufficiently large, by letting $\triangle\vartheta = (\vartheta_M - \vartheta_1)/M = 2\pi/M$ and applying (3.6) and (3.7), it yields

$$\begin{aligned}\sum_{m=1}^{M} G(\mathbf{r}, \mathbf{a}_m)\overline{G(\mathbf{r}', \mathbf{a}_m)} &= \frac{M}{M\triangle\vartheta}\sum_{m=1}^{M}\frac{2}{k_{\mathrm{b}}|\mathbf{a}_m|\pi}e^{ik_{\mathrm{b}}\boldsymbol{\vartheta}_m\cdot(\mathbf{r}'-\mathbf{r})}\triangle\vartheta\\ &\approx \frac{2M}{k_{\mathrm{b}}|\mathbf{a}|\pi(2\pi)}\int_{\mathbb{S}^1} e^{ik_{\mathrm{b}}\boldsymbol{\vartheta}\cdot(\mathbf{r}'-\mathbf{r})}\mathrm{d}\boldsymbol{\vartheta}\\ &= \frac{2M}{k_{\mathrm{b}}|\mathbf{a}|\pi}\left(\frac{1}{2\pi}\int_0^{2\pi} e^{ik_{\mathrm{b}}|\mathbf{r}'-\mathbf{r}|\cos(\vartheta-\phi)}\mathrm{d}\vartheta\right) \approx \frac{2M}{k_{\mathrm{b}}|\mathbf{a}|\pi}J_0(k_{\mathrm{b}}|\mathbf{r}'-\mathbf{r}|)\end{aligned} \tag{5.2}$$

and

$$\begin{aligned}&\sum_{m=1}^{M} G(\mathbf{r}, \mathbf{a}_m)\overline{G(\mathbf{a}_m, \mathbf{r})}\cos\left(p(\vartheta_m - \phi)\right)\\ &\approx \frac{2M}{k_{\mathrm{b}}|\mathbf{a}|\pi(2\pi)}\int_0^{2\pi}\cos\left(p(\vartheta-\phi)\right)e^{ik_{\mathrm{b}}|\mathbf{r}'-\mathbf{r}|\cos(\vartheta-\phi)}\mathrm{d}\vartheta\\ &\approx \frac{M}{k_{\mathrm{b}}|\mathbf{a}|\pi^2}\int_0^{2\pi}\cos\left(p(\vartheta-\phi)\right)\Big(J_0(k_{\mathrm{b}}|\mathbf{r}'-\mathbf{r}|) + 2\sum_{q=1}^{\infty} i^q J_q(k_{\mathrm{b}}|\mathbf{r}'-\mathbf{r}|)\cos\left(q(\vartheta-\phi)\right)\Big)\mathrm{d}\vartheta\\ &= \frac{2Mi^p}{k_{\mathrm{b}}|\mathbf{a}|\pi}J_p(k_{\mathrm{b}}|\mathbf{r}'-\mathbf{r}|).\end{aligned} \tag{5.3}$$

In addition, based on (5.2) and (5.3), we can examine that

$$\begin{aligned}&\sum_{m=1}^{M} G(\mathbf{r}, \mathbf{a}_m)\overline{G(\mathbf{a}_m, \mathbf{r})}\left[J_0(k_{\mathrm{b}}|\mathbf{r}'-\mathbf{r}|) + \frac{3}{\pi}\mathcal{E}(\mathbf{r}', \mathbf{r}, \mathbf{a}_m)\right]\\ &\qquad\approx \frac{2M}{k_{\mathrm{b}}|\mathbf{a}|\pi}\left[J_0(k_{\mathrm{b}}|\mathbf{r}'-\mathbf{r}|)^2 + \frac{3}{\pi}\sum_{p=1}^{\infty}\frac{i^p}{p}J_p(k_{\mathrm{b}}|\mathbf{r}'-\mathbf{r}|)^2\sin\left(\frac{2p}{3}\pi\right)\right]\end{aligned}$$

and immediately derive (5.1). □

According to Theorem 5.1, we can examine some properties of the indicator function $\mathfrak{F}_{\mathrm{MOSM}}(\mathbf{r}')$.

Remark 5.1 (Availability of object detection). Similar to Remark 3.2, the resulting plot of the indicator function $\mathfrak{F}_{\mathrm{MOSM}}(\mathbf{r}')$ is expected to exhibit peaks of magnitudes $\frac{2}{3|\mathbf{a}||\mathbf{b}|}\left(\frac{\varepsilon_s-\varepsilon_0}{\varepsilon_0\mu_0}\right)\mathrm{area}(D_s)$ at the $\mathbf{r}' = \mathbf{r} \in D_s$ sought. Note that opposite to the single source case, the imaging performance is independent of the emitters' and receivers' locations; thus, it will be possible to recognize the existence or outline shape of the objects through the map of $\mathfrak{F}_{\mathrm{MOSM}}(\mathbf{r}')$.

Remark 5.2 (Effect of the factor $\mathcal{M}(\mathbf{r}', \mathbf{r})$). Similar to the OSM with a single source, the factor $\mathcal{M}(\mathbf{r}', \mathbf{r})$ of (5.1) will generate some artifacts. Moreover, it does not contribute to the identification of objects; however, it fortunately does not disturb object detection. To examine the influence of the $\mathcal{M}(\mathbf{r}', \mathbf{r})$, we consider the following quantity:

$$\mathcal{D}_2(x) = \left|J_0(k_{\mathrm{b}}|x|)^2 + \frac{3}{\pi}\sum_{p=1}^{10^6}\frac{i^p}{p}J_p(k_{\mathrm{b}}|x|)^2\sin\left(\frac{2p}{3}\pi\right)\right|.$$

Note that this is a one-dimensional version of $|J_0(k_b|\mathbf{r}' - \mathbf{r}|)^2 + \frac{3}{\pi}\mathcal{M}(\mathbf{r}', \mathbf{r})|$ for $\mathbf{r} = (0, 0)$. In contrast to Remark 3.4, we can say that although $\mathcal{M}(\mathbf{r}', \mathbf{r})$ generates some artifacts, it successfully cancels out certain artifacts generated by the factor $J_0(k_b|\mathbf{r}' - \mathbf{r}|)^2$. Therefore, we can conclude that the factor $\mathcal{M}(\mathbf{r}', \mathbf{r})$ contributes to making the background cleaner and, correspondingly, improving the reconstruction. Refer to Figure 12.

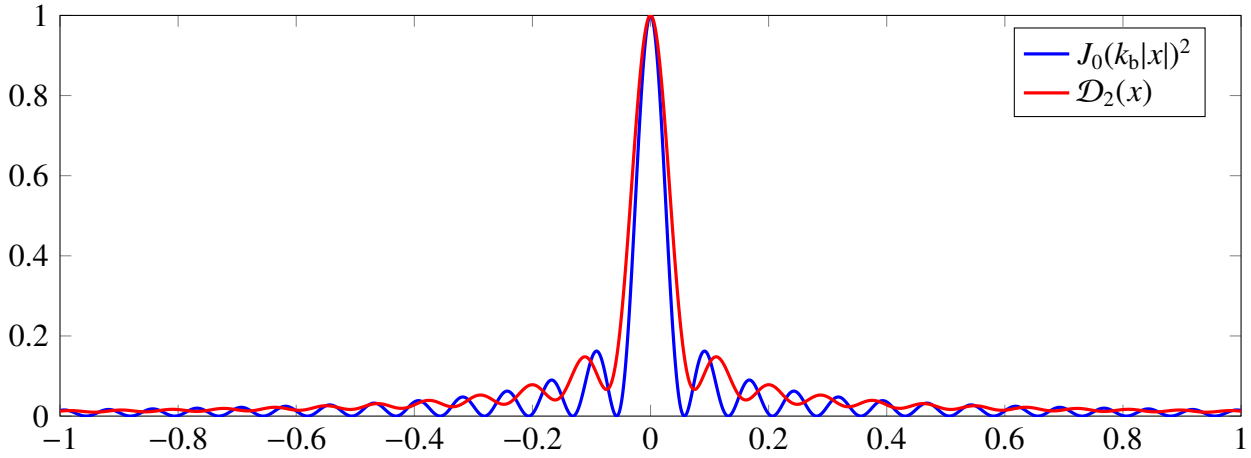

Figure 12. Plots of $J_0(k_b|x|)^2$ and $\mathcal{D}_2(x)$ for $-1 \le x \le 1$ and $f = 2$ GHz.

Remark 5.3 (Comparing imaging performance with a single source OSM). Here, we compare the imaging performance of the OSM with single and multiple sources. By referring to the 1D plots of $\mathfrak{F}_{\mathrm{OSM}}(\mathbf{r}', \mathbf{a}_1)$ and $\mathfrak{F}_{\mathrm{MOSM}}(\mathbf{r}')$ for $\mathbf{r}' = (x, 0)$ with $-1 \le x \le 1$ in Figure 13, we conclude that the $\mathfrak{F}_{\mathrm{MOSM}}(\mathbf{r}')$ yields better quality images due to less oscillation than $\mathfrak{F}_{\mathrm{OSM}}(\mathbf{r}', \mathbf{a}_m)$. A more detailed description is given as follows: Since $\mathcal{E}(\mathbf{r}', \mathbf{r}, \mathbf{a}_m)$ and $\mathcal{M}(\mathbf{r}', \mathbf{r})$ are uniformly convergent, for each $\epsilon > 0$, there exists a natural number $P = P(\epsilon)$ such that

$$\left|\mathcal{E}(\mathbf{r}', \mathbf{r}, \mathbf{a}_m) - \sum_{p=1}^{P} \frac{(-i)^p}{p} J_p(k_b|\mathbf{r}' - \mathbf{r}|) \cos\left(p(\vartheta_m - \phi)\right) \sin\left(\frac{2p}{3}\pi\right)\right| < \epsilon$$

and

$$\left|\mathcal{M}(\mathbf{r}', \mathbf{r}) - \sum_{p=1}^{P} \frac{i^p}{p} J_p(k_b|\mathbf{r}' - \mathbf{r}|)^2 \sin\left(\frac{2p}{3}\pi\right)\right| < \epsilon.$$

Suppose that $\mathbf{r}'$ is not close to $\mathbf{r}$ such that $k_b|\mathbf{r}' - \mathbf{r}| \gg 1/4$. Then, since the following asymptotic form holds:

$$J_p(k_b|\mathbf{r}' - \mathbf{r}|) \approx \sqrt{\frac{2}{k_b\pi|\mathbf{r}' - \mathbf{r}|}} \cos\left(k_b|\mathbf{r}' - \mathbf{r}| - \frac{p\pi}{2} - \frac{\pi}{4} + O\left(\frac{1}{k_b|\mathbf{r}' - \mathbf{r}|}\right)\right),$$

applying the Euler–Maclaurin formula yields

$$|\mathcal{E}(\mathbf{r}', \mathbf{r}, \mathbf{a}_m)| \le \left|\sum_{p=1}^{P} \frac{(-i)^p}{p} \sqrt{\frac{2}{k_b\pi|\mathbf{r}' - \mathbf{r}|}} \cos\left(k_b|\mathbf{r}' - \mathbf{r}| - \frac{p\pi}{2} - \frac{\pi}{4} + O\left(\frac{1}{k_b|\mathbf{r}' - \mathbf{r}|}\right)\right) \sin\left(\frac{2p}{3}\pi\right)\right|$$

$$\leq \sqrt{\frac{3}{2k_{\mathrm{b}}\pi|\mathbf{r}'-\mathbf{r}|}}\sum_{p=1}^{P}\frac{1}{p} = \sqrt{\frac{3}{2k_{\mathrm{b}}\pi|\mathbf{r}'-\mathbf{r}|}}\left(\ln P+\gamma+\frac{1}{2P}-c_p\right)$$
$$\leq \sqrt{\frac{3}{2k_{\mathrm{b}}\pi|\mathbf{r}'-\mathbf{r}|}}\left(\ln P+\gamma+\frac{1}{2P}\right)$$

and

$$|\mathcal{M}(\mathbf{r}',\mathbf{r})| \approx \left|\sum_{p=1}^{P}\frac{i^p}{p}\frac{2}{k_{\mathrm{b}}\pi|\mathbf{r}'-\mathbf{r}|}\cos^2\left(k_{\mathrm{b}}|\mathbf{r}'-\mathbf{r}|-\frac{p\pi}{2}-\frac{\pi}{4}+O\left(\frac{1}{k_{\mathrm{b}}|\mathbf{r}'-\mathbf{r}|}\right)\right)\sin\left(\frac{2p}{3}\pi\right)\right|$$
$$\leq \frac{\sqrt{3}}{k_{\mathrm{b}}\pi|\mathbf{r}'-\mathbf{r}|}\sum_{p=1}^{P}\frac{1}{p} \leq \frac{\sqrt{3}}{k_{\mathrm{b}}|\mathbf{r}'-\mathbf{r}|}\left(\ln P+\gamma+\frac{1}{2P}\right),$$

where c_p satisfies $0 \leq c_p \leq (8p^2)^{-1}$ and $\gamma = 0.577215665\ldots$ denotes the Euler–Mascheroni constant. Therefore, since $(k_{\mathrm{b}}|\mathbf{r}'-\mathbf{r}|)^{-1} \ll O(1)$, we can say that the values of $\mathcal{E}(\mathbf{r}',\mathbf{r},\mathbf{a}_m)$ and $\mathcal{M}(\mathbf{r}',\mathbf{r})$ are negligible if the search point is far away from the object.

Now, assume that $\mathbf{r}'$ is close to $\mathbf{r}$ such that $0 < k_{\mathrm{b}}|\mathbf{r}'-\mathbf{r}| \ll \sqrt{P+1}$. In this case, based on the asymptotic form of the Bessel function

$$J_p(k_{\mathrm{b}}|\mathbf{r}'-\mathbf{r}|) \approx \frac{1}{\Gamma(p+1)}\left(\frac{k_{\mathrm{b}}|\mathbf{r}'-\mathbf{r}|}{2}\right)^p,$$

we can examine that

$$|\mathcal{E}(\mathbf{r}',\mathbf{r},\mathbf{a}_m)| \approx \left|\sum_{p=1}^{P}\frac{(-i)^p}{p\Gamma(p+1)}\left(\frac{k_{\mathrm{b}}|\mathbf{r}'-\mathbf{r}|}{2}\right)^p\cos\left(p(\vartheta_m-\phi)\right)\sin\left(\frac{2p}{3}\pi\right)\right| \leq \sum_{p=1}^{P}\frac{(k_{\mathrm{b}}|\mathbf{r}'-\mathbf{r}|)^p}{p2^p\Gamma(p+1)} := \sum_{p=1}^{P}a_p$$

and

$$|\mathcal{M}(\mathbf{r}',\mathbf{r})| \approx \left|\sum_{p=1}^{P}\frac{i^p}{p\Gamma(p+1)^2}\left(\frac{k_{\mathrm{b}}|\mathbf{r}'-\mathbf{r}|}{2}\right)^{2p}\cos\left(p(\vartheta_m-\phi)\right)\sin\left(\frac{2p}{3}\pi\right)\right| \leq \sum_{p=1}^{P}\frac{(k_{\mathrm{b}}|\mathbf{r}'-\mathbf{r}|)^{2p}}{p2^{2p}\Gamma(p+1)^2} := \sum_{p=1}^{P}b_p,$$

where $\Gamma(p) = (p-1)!$ denotes the Gamma function. Since

$$\lim_{p\to\infty}\frac{b_p}{a_p} = \lim_{p\to\infty}\frac{(k_{\mathrm{b}}|\mathbf{r}'-\mathbf{r}|)^p}{2^p\Gamma(p+1)} \ll \lim_{p\to\infty}\frac{(\sqrt{P+1})^p}{2^p\Gamma(p+1)} = 0,$$

it is possible to say that the factor $\mathcal{M}(\mathbf{r}',\mathbf{r})$ generates fewer artifacts than $\mathcal{E}(\mathbf{r}',\mathbf{r},\mathbf{a}_m)$ because $\mathcal{M}(\mathbf{r}',\mathbf{r})$ has a smaller amplitude than $\mathcal{E}(\mathbf{r}',\mathbf{r},\mathbf{a}_m)$. We refer to Figures 2 and 12 for the 1D plots of $\mathcal{D}_1(x)$ and $\mathcal{D}_2(x)$, respectively.

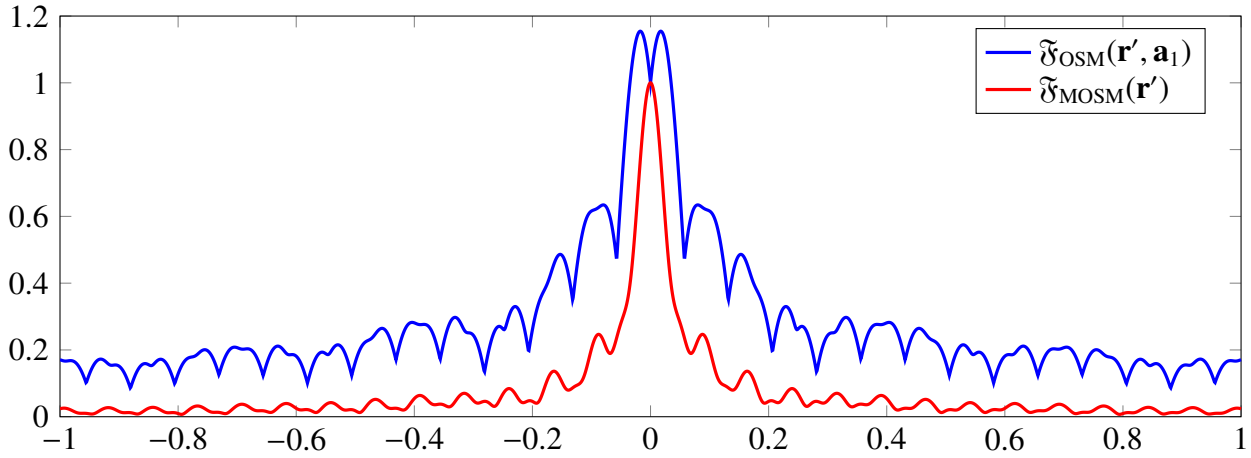

Figure 13. 1D plots of $\mathfrak{F}_{\mathrm{OSM}}(\mathbf{r}', \mathbf{a}_1)$ and $\mathfrak{F}_{\mathrm{MOSM}}(\mathbf{r}')$ for $\mathbf{r} = (0, 0)$ and $\mathbf{r}' = (x, 0)$, $-1 \leq x \leq 1$, at $f = 2\,\mathrm{GHz}$.

Remark 5.4 (Unique identification of the objects). Following Theorem 5.1 and Remarks 5.1 and 5.3, the value of $\mathfrak{F}_{\mathrm{MOSM}}(\mathbf{r}')$ will reach its local maxima when $\mathbf{r}' \in D$. Hence, small objects can be uniquely identified through the map of $\mathfrak{F}_{\mathrm{MOSM}}(\mathbf{r}')$.

6. Simulation results with synthetic and Fresnel experimental database

In this section, we exhibit some numerical simulation results with synthetic and Fresnel experimental database. Note that the simulation configuration is same as that described in Section 4, except the range of emitters is 0° to 350° with a step size of 10°. To compare the accuracy of the imaging results, we evaluated the Jaccard index, which measures the similarity between two finite sets A and B. Refer to [64]. It is defined as

$$\mathcal{J}[A, B](\%) = \frac{|A \cap B|}{|A \cup B|} \times 100\%.$$

Here, the Jaccard index is calculated by comparing

$$A = \begin{cases} \mathfrak{F}(\mathbf{r}') & \text{if} \quad \mathfrak{F}(\mathbf{r}') \geq \zeta \\ 0 & \text{if} \quad \mathfrak{F}(\mathbf{r}') < \zeta \end{cases} \quad \text{and} \quad B = \frac{|\varepsilon(\mathbf{r}') - \varepsilon_0|}{\max\limits_{\mathbf{r} \in \Omega} |\varepsilon(\mathbf{r}') - \varepsilon_0|},$$

where ζ denotes the threshold such that $0 \leq \zeta \leq 1$ and $\mathfrak{F}(\mathbf{r}')$ is either $\mathfrak{F}_{\mathrm{OSMM}}(\mathbf{r}')$ or $\mathfrak{F}_{\mathrm{MOSM}}(\mathbf{r}')$. In this case, performing all the numerical experiments took approximately 4.35 seconds, which is about three times longer than in the single source case.

Example 6.1 (Imaging results with synthetic data). Figure 14 shows the maps of $\mathfrak{F}_{\mathrm{OSMM}}(\mathbf{r}')$, $\mathfrak{F}_{\mathrm{MOSM}}(\mathbf{r}')$, and the Jaccard index at $f = 1, 2\,\mathrm{GHz}$. Although the existence of D_2 can be recognized, it is impossible to identify D_1 and D_3 through the maps of $\mathfrak{F}_{\mathrm{OSMM}}(\mathbf{r}')$ and $\mathfrak{F}_{\mathrm{MOSM}}(\mathbf{r}')$ at $f = 1\,\mathrm{GHz}$. Fortunately, in contrast to the single source case, the existence and location of the three objects can be retrieved successfully at $f = 2\,\mathrm{GHz}$. Let us notice that, based on the evaluated Jaccard index and appearance of several artifacts, the imaging performance of $\mathfrak{F}_{\mathrm{MOSM}}(\mathbf{r}')$ is better than that of $\mathfrak{F}_{\mathrm{OSM}}(\mathbf{r}')$. A similar phenomenon can be examined in the imaging results shown in Figures 15 and 16 at $f = 3, 4, 6\,\mathrm{GHz}$.

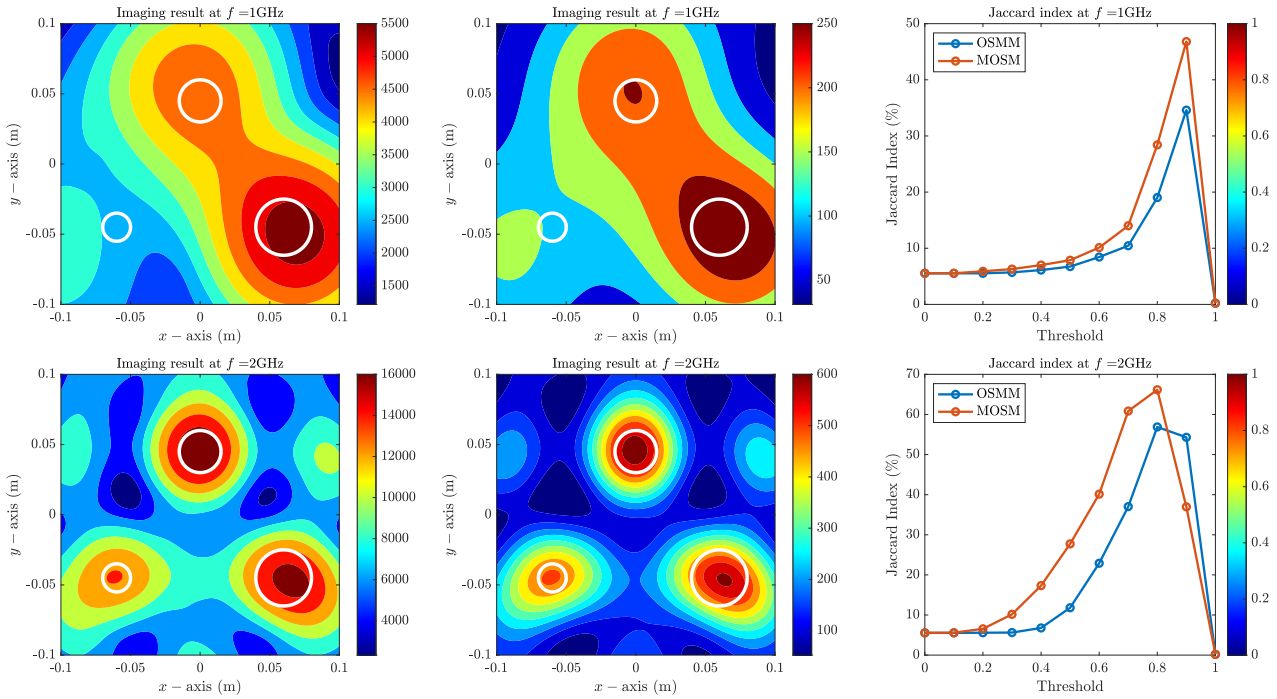

Figure 14. (Example 6.1) Maps of $\mathfrak{F}_{\text{OSMM}}(\mathbf{r}')$ (left column) and $\mathfrak{F}_{\text{MOSM}}(\mathbf{r}')$ (middle column), as well as the Jaccard index versus the threshold (right column) at $f = 1, 2$ GHz.

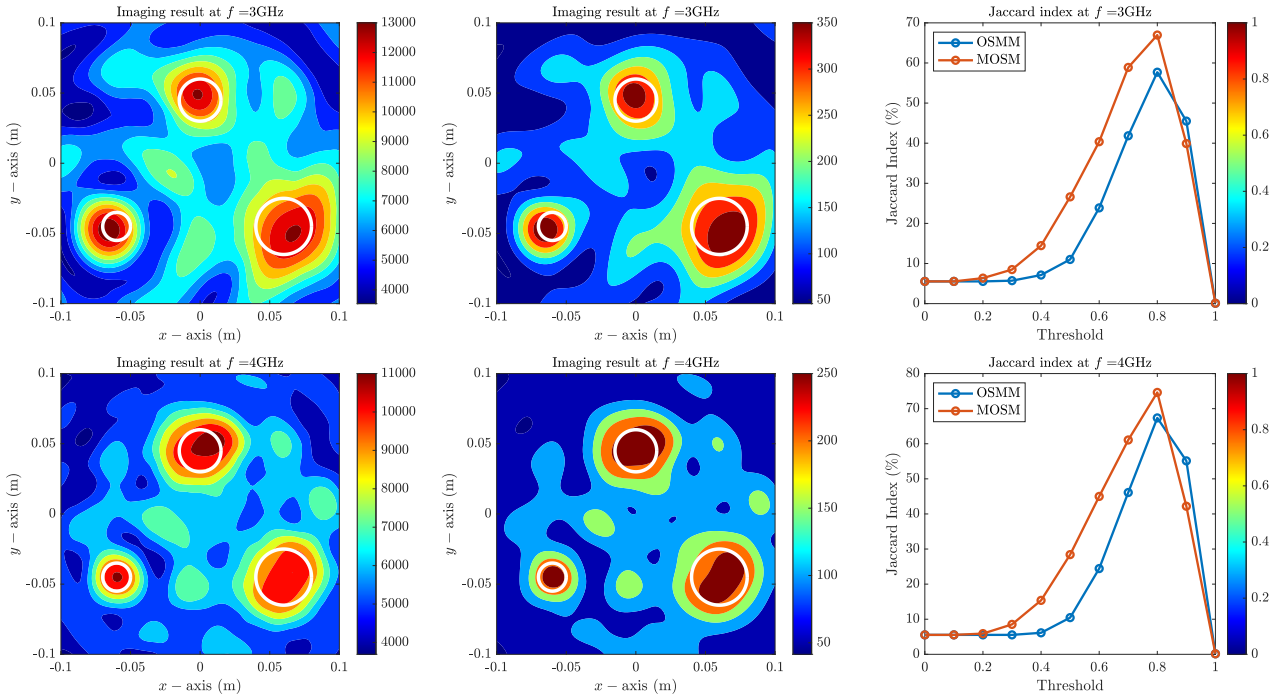

Figure 15. (Example 6.1) Maps of $\mathfrak{F}_{\text{OSMM}}(\mathbf{r}')$ (left column) and $\mathfrak{F}_{\text{MOSM}}(\mathbf{r}')$ (middle column), as well as the Jaccard index versus the threshold (right column) at $f = 3, 4$ GHz.

In contrast to the previous results, it is possible to recognize the existence of three objects, but peaks of large magnitudes have appeared along the boundaries of the objects. Refer to Remark 2.1. Thus, similar to Remark 3.2, applying an extremely high frequency seems inappropriate to retrieve unknown objects.

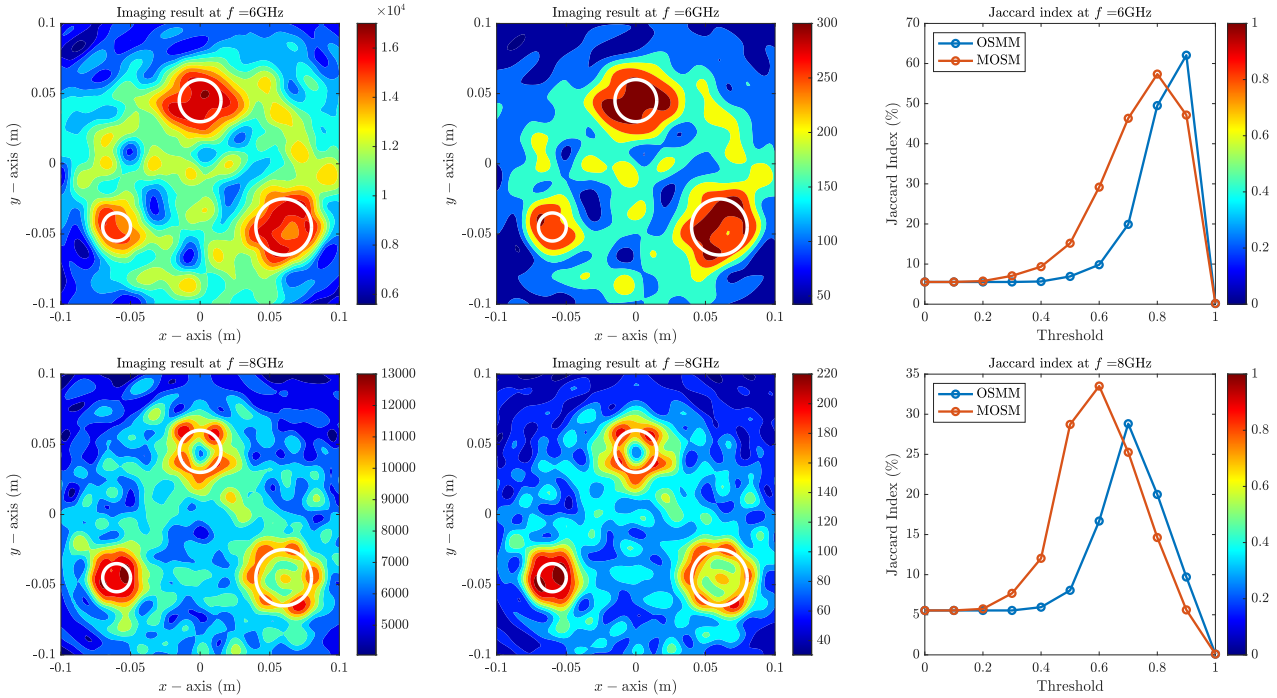

Figure 16. (Example 6.1) Maps of $\mathfrak{F}_{\mathrm{OSMM}}(\mathbf{r}')$ (left column) and $\mathfrak{F}_{\mathrm{MOSM}}(\mathbf{r}')$ (middle column), as well as the Jaccard index versus the threshold (right column) at $f = 6, 8$ GHz.

Example 6.2 (Imaging results with Fresnel database). Figure 17 shows the maps of $\mathfrak{F}_{\mathrm{OSMM}}(\mathbf{r}')$, $\mathfrak{F}_{\mathrm{MOSM}}(\mathbf{r}')$, and the Jaccard index at $f = 1, 2$ GHz. As with the imaging result with the single source, it is impossible to recognize two objects through the maps of $\mathfrak{F}_{\mathrm{OSMM}}(\mathbf{r}')$ and $\mathfrak{F}_{\mathrm{MOSM}}(\mathbf{r}')$ at $f = 1$ GHz. Fortunately, in contrast to the single source case, the location and outline shape of the two objects can be retrieved successfully at $f = 2$ GHz. Although the imaging quality of $\mathfrak{F}_{\mathrm{OSMM}}(\mathbf{r}')$ and $\mathfrak{F}_{\mathrm{MOSM}}(\mathbf{r}')$ appears to be similar, based on the evaluated Jaccard index, the imaging performance of $\mathfrak{F}_{\mathrm{MOSM}}(\mathbf{r}')$ is slightly better than that of $\mathfrak{F}_{\mathrm{OSM}}(\mathbf{r}')$. Note that a similar phenomenon can be observed in the imaging results shown in Figure 18 at $f = 3, 4$ GHz.

Opposite to the imaging results with a single source, it is possible to recognize the existence of two objects at $f = 6, 8$ GHz (refer to Figure 19). However, the imaging quality appears to be poorer than that shown in Figure 18, as peaks of large magnitudes have appeared along the boundaries of the objects. Refer to Remark 2.1. Thus, similar to Remark 3.2, applying an extremely high frequency seems inappropriate to retrieve unknown objects.

Figure 20 shows the maps of $\mathfrak{F}_{\mathrm{MOSM}}(\mathbf{r}')$ at several frequencies when the measured scattered-field data were contaminated with 15 dB white Gaussian random noise. Similar to the imaging with a single source, a comparison of the results in Figures 17, 18, and 19 shows that the imaging results are very similar, indicating that the OSM with multiple sources is robust to random noise.

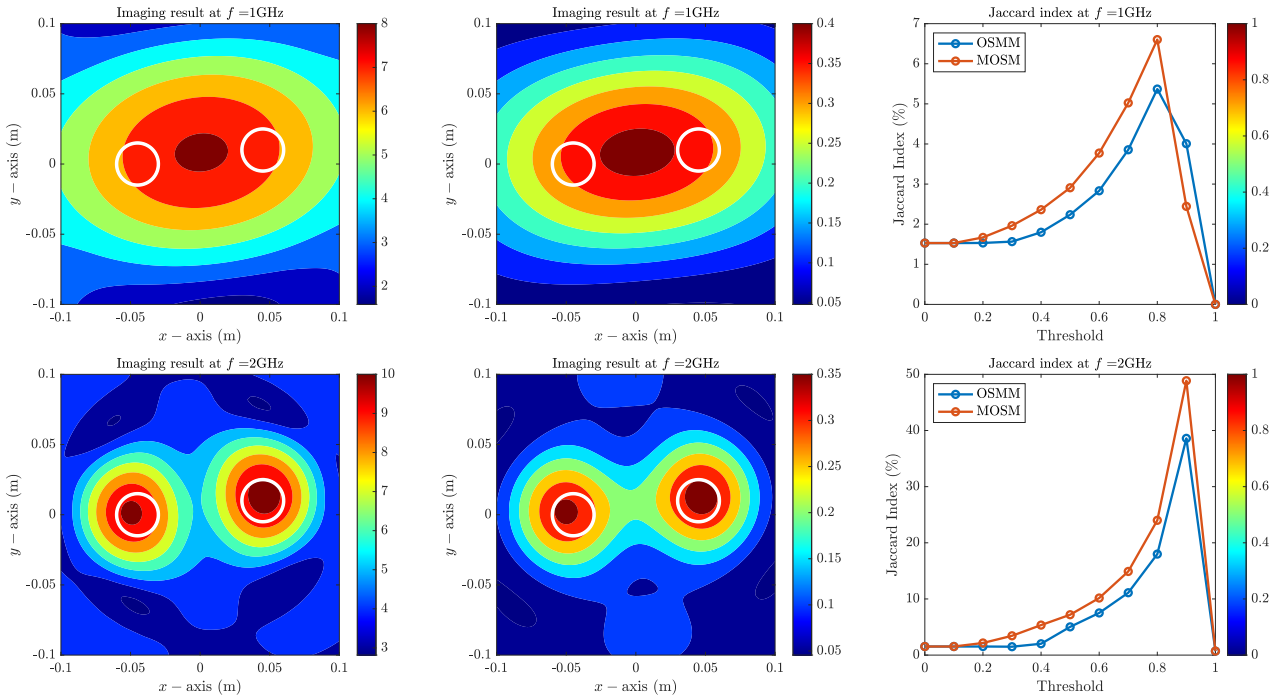

Figure 17. (Example 6.2) Maps of $\mathfrak{F}_{\text{OSMM}}(\mathbf{r}')$ (left column) and $\mathfrak{F}_{\text{MOSM}}(\mathbf{r}')$ (middle column), as well as the Jaccard index versus the threshold (right column) at $f = 1, 2$ GHz.

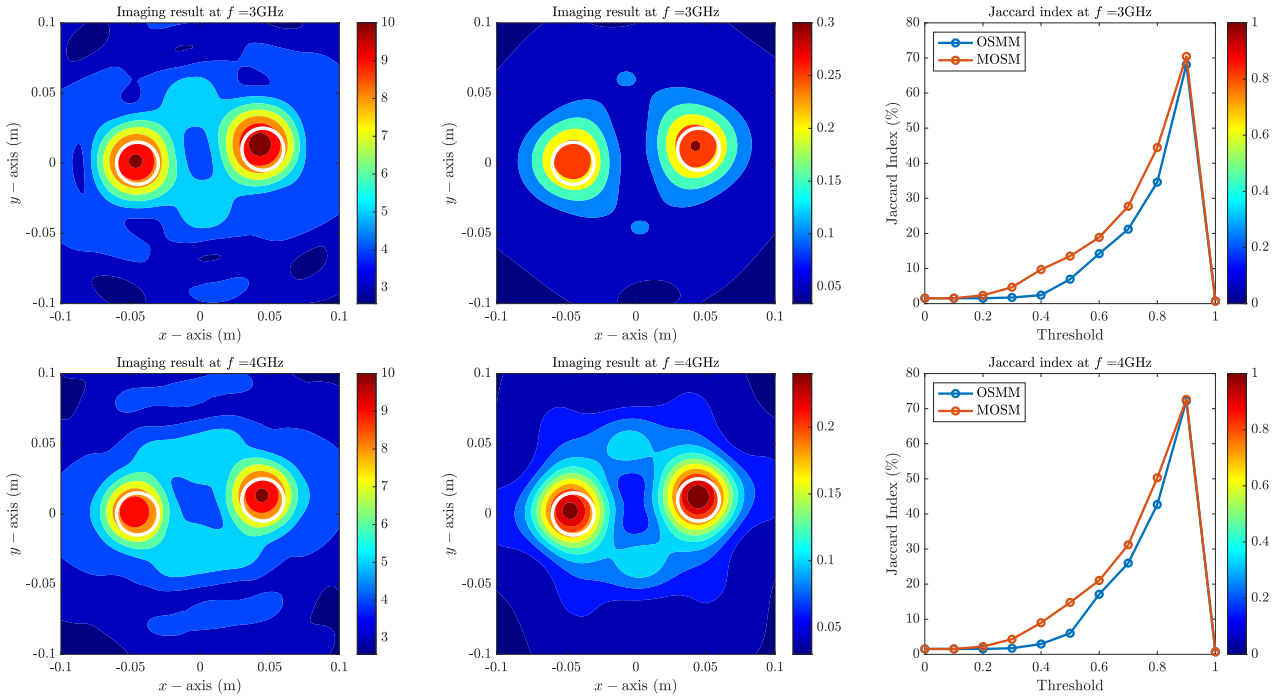

Figure 18. (Example 6.2) Maps of $\mathfrak{F}_{\text{OSMM}}(\mathbf{r}')$ (left column) and $\mathfrak{F}_{\text{MOSM}}(\mathbf{r}')$ (middle column), as well as the Jaccard index versus the threshold (right column) at $f = 3, 4$ GHz.

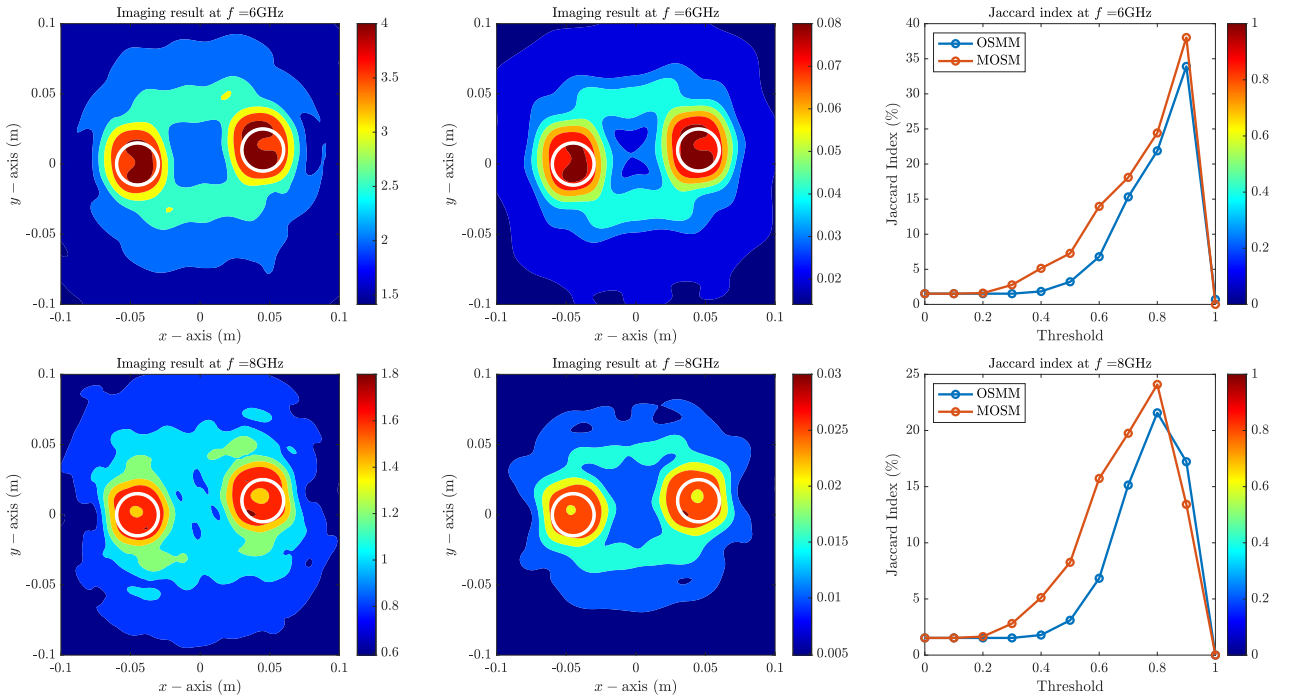

Figure 19. (Example 6.2) Maps of $\mathfrak{F}_{\text{OSMM}}(\mathbf{r}')$ (left column) and $\mathfrak{F}_{\text{MOSM}}(\mathbf{r}')$ (middle column), as well as the Jaccard index versus the threshold (right column) at $f = 6, 8$ GHz.

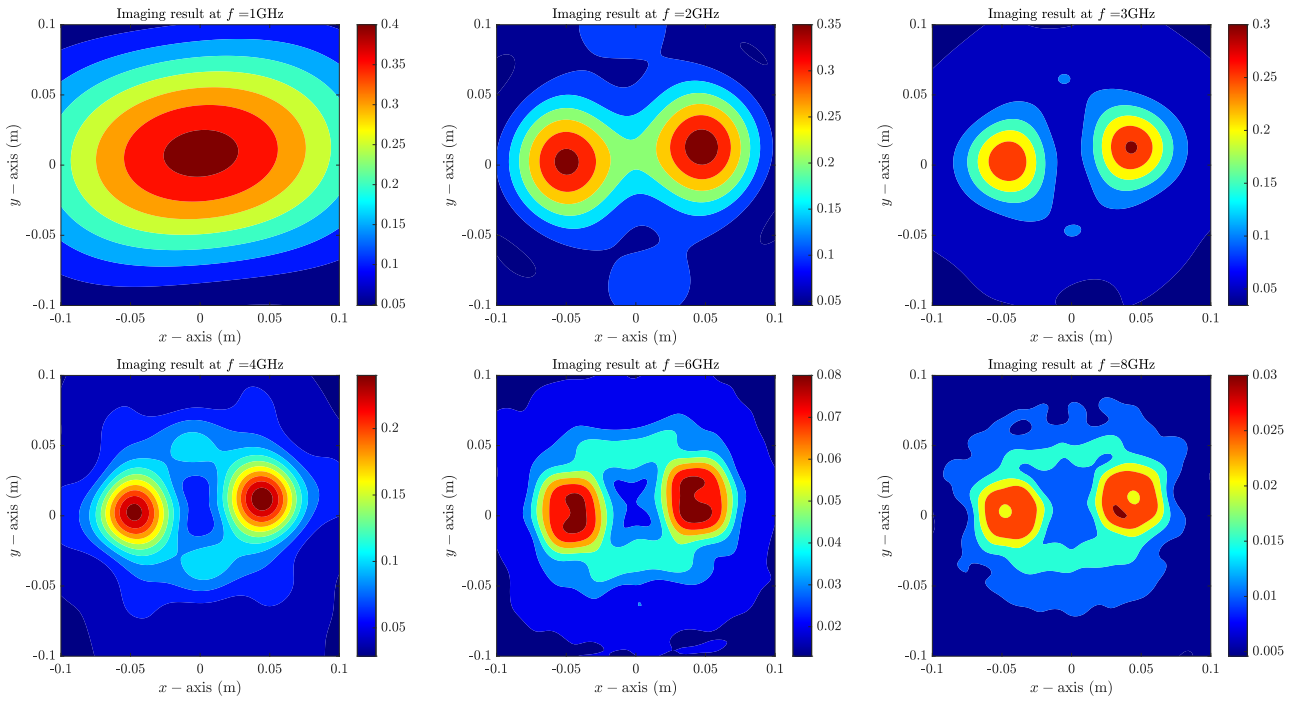

Figure 20. (Example 6.2) Maps of $\mathfrak{F}_{\text{MOSM}}(\mathbf{r}')$ with noisy data.

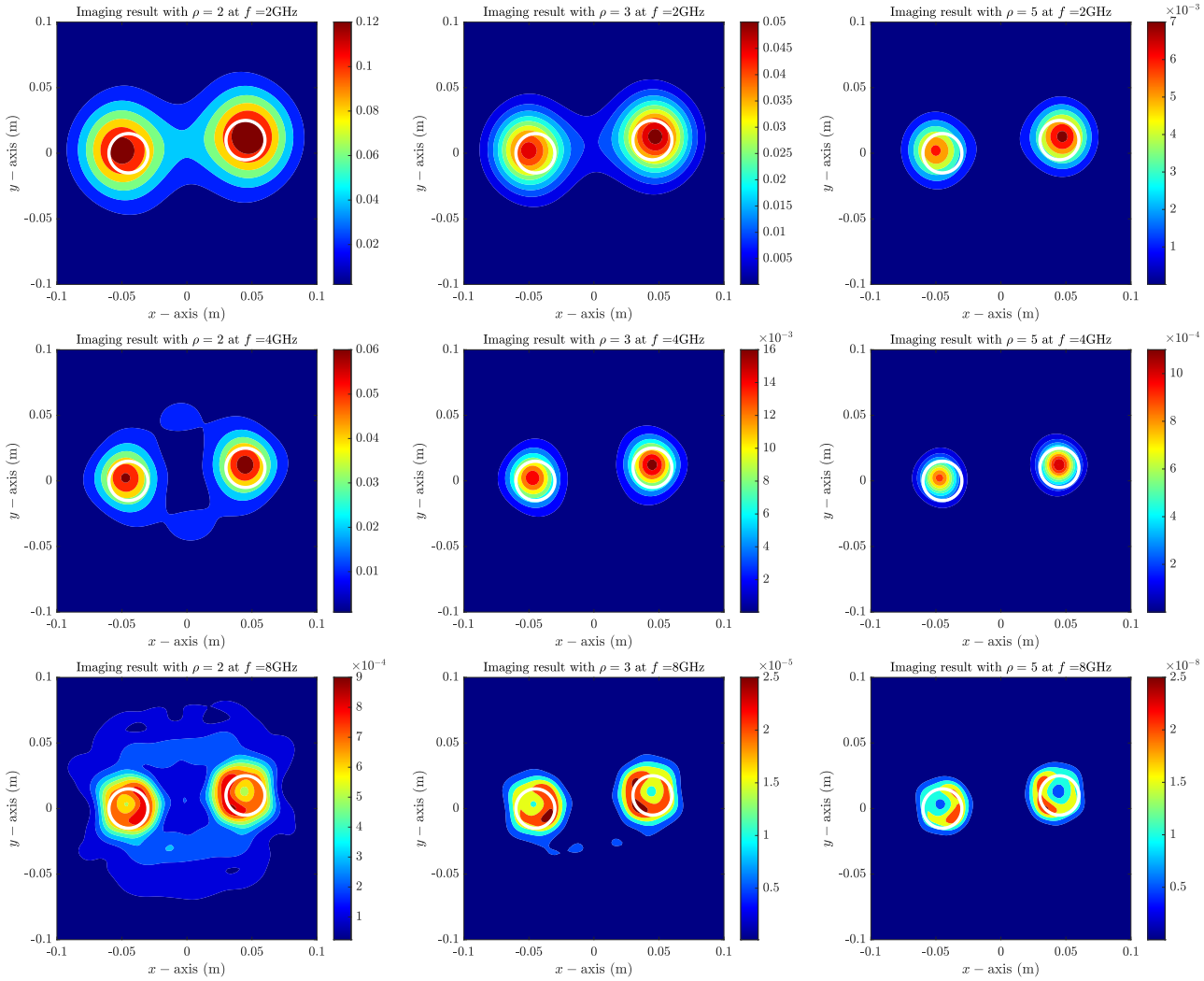

Figure 21. (Example 6.3) Maps of $\mathfrak{F}_{\mathrm{OSMP}}(\mathbf{r}', \rho)$ with $\rho = 2$ (left column), $\rho = 3$ (middle columm), and $\rho = 5$ (right column) at $f = 2, 4, 8$ GHz.

Example 6.3 (Imaging results with multiple sources: further result). For the final example, we consider the following indicator function with multiple sources, incorporating the power of ρ (see [62]): for each $\mathbf{r}' \in \Omega$,

$$\mathfrak{F}_{\mathrm{OSMP}}(\mathbf{r}', \rho) = \left(\mathfrak{F}_{\mathrm{MOSM}}(\mathbf{r}')\right)^{\rho} = \left| \sum_{m=1}^{M} \Phi(\mathbf{r}', \mathbf{a}_m) \overline{G(\mathbf{r}', \mathbf{a}_m)} \right|^{\rho}.$$

Then, based on Theorem 5.1, we immediately observe that

$$\mathfrak{F}_{\mathrm{OSMP}}(\mathbf{r}', \rho) = \left| \frac{MN}{4|\mathbf{a}||\mathbf{b}|\pi^2} \int_D \left(\frac{\varepsilon(\mathbf{r}) - \varepsilon_0}{\varepsilon_0 \mu_0} \right) \left(J_0(k_{\mathrm{b}}|\mathbf{r}' - \mathbf{r}|)^2 + \frac{3}{\pi} \mathcal{M}(\mathbf{r}', \mathbf{r}) \right) \mathrm{d}\mathbf{r} \right|^{\rho},$$

where $\mathcal{M}(\mathbf{r}', \mathbf{r})$ is defined in (5.1). Notice that, referring Remark 5.2, we have

$$\left| J_0(k_{\mathrm{b}}|\mathbf{r}' - \mathbf{r}|)^2 + \frac{3}{\pi} \mathcal{M}(\mathbf{r}', \mathbf{r}) \right|^{\rho} = \begin{cases} 1 & \text{if} \quad \mathbf{r}' \in D, \\ a^{\rho} & \text{if} \quad \mathbf{r}' \in \Omega \backslash \overline{D}, \end{cases}$$

where $a \in \mathbb{R}$ satisfies $0 < a < 1$. Since $a^\rho \longrightarrow 0$ as $\rho \longrightarrow +\infty$, we expect that several artifacts in the map of $\mathfrak{F}_{\text{OSMP}}(\mathbf{r}', \rho)$ can be mitigated when ρ is sufficiently large.

Figure 21 shows the maps of $\mathfrak{F}_{\text{OSMP}}(\mathbf{r}', \rho)$ with various ρ and frequencies of operation. By comparing the results in Figures 17 18, and 19, it is very easy to recognize the existence and outline shapes of the objects because several artifacts were mitigated when $\rho = 3, 5$.

Remark 6.1. Let us emphasize that the objects D_1 and D_2 are almost identical. Thus, several artifacts can be successfully eliminated for sufficiently large ρ. However, if the material property (size, permittivity, or conductivity) of an object (say D_1) is smaller than another one (say D_2), the value of $\mathfrak{F}_{\text{OSMP}}(\mathbf{r}', \rho)$ on D_1 becomes extremely smaller than the one on D_2 so that it will be very hard to identify the existence and location of D_1.

7. Conclusion

This paper has considered the application of the OSM with a single source to identify the existence and outline shape of small dielectric objects from real-world experimental data. Thanks to the asymptotic expansion formula for the scattered field data in the presence of small objects, we derived an accurate relationship between the indicator function and an infinite series of the Bessel function of the first kind. Based on this derived relationship, we investigated various properties of the indicator function, including its applicability and limitations. In addition, we have verified the theoretical results with experimental data at various frequencies.

To improve the imaging performance of the OSM, we collected scattered field data with multiple sources and proposed a new indicator function. Through careful analysis, we have demonstrated that the imaging performance of the proposed indicator function is independent of the emitter location and outperforms the traditional OSM with single and multiple sources. We have demonstrated, as confirmed in Remarks 2.1 and 2.2, that it is possible to identify small objects uniquely if the applied frequency is not extremely low or high. However, as demonstrated in Example 6.3, increasing the power ρ reduces unexpected artifacts, but it becomes difficult to image small-size/low-dielectric-constant objects.

In this study, we considered the application of the OSM using transverse magnetic polarized waves included in the 2D Fresnel experimental dataset. Application and analysis of the OSM using transverse electric polarized waves will be the forthcoming work. Furthermore, an extension to the 3D Fresnel experimental database [47, 65] will be an interesting and remarkable research topic. It should be noted that good imaging results can be obtained using the designed MOSM. Therefore, it is expected that this can be further applied to identify unknown objects from sparse data in future studies. Finally, this study concerned the application of the OSM in the frequency-domain inverse scattering problem. Based on recent studies [66, 67], we believe that the approach considered in this study can be adapted to the time-domain sampling method, and this will also be an interesting topic for future research.

Use of Generative-AI tools declaration

The author declares he has not used Artificial Intelligence (AI) tools in the creation of this article.

Acknowledgments

The author would like to thank the anonymous reviewers for their valuable comments, which have helped improve the quality of the paper. This research was supported by the National Research Foundation of Korea (NRF) grant funded by the Korea government (MSIT) (RS-2025-16067902) and the research program of Kookmin University.

Conflict of interest

The author declare there is no conflict of interest.

References

1. H. Ammari, An Introduction to Mathematics of Emerging Biomedical Imaging, In: *Mathematics and Applications Series,* Springer, Berlin, 2008.
2. H. Ammari, Mathematical Modeling in Biomedical Imaging II: Optical, Ultrasound, and Opto-Acoustic Tomographies, In: *Lecture Notes in Mathematics,* Springer, Berlin, 2011. https://doi.org/10.1007/978-3-642-22990-9
3. S. Coşğun, E. Bilgin, M. Çayören, Microwave imaging of breast cancer with factorization method: SPIONs as contrast agent, *Med. Phys.*, **47** (2020), 3113–3122. https://doi.org/10.1002/mp.14156
4. N. Simonov, B.-R. Kim, K.-J. Lee, S.-I. Jeon, S.-H. Son, Advanced fast 3-D electromagnetic solver for microwave tomography imaging, *IEEE Trans. Med. Imag.*, **36** (2017), 2160–2170. https://doi.org/10.1109/TMI.2017.2712800
5. E. J. Baranoski, Through-wall imaging: Historical perspective and future directions, *J. Franklin Inst.*, **345** (2008), 556–569. https://doi.org/10.1016/j.jfranklin.2008.01.005
6. F. Soldovieri, R. Solimene, F. Ahmad, Sparse tomographic inverse scattering approach for through-the-wall radar imaging, *IEEE Trans. Instrum. Meas.*, **61** (2012), 3340–3350. https://doi.org/10.1109/TIM.2012.2210454
7. M. Q. Feng, F. D. Flaviis, Y. J. Kim, Use of microwaves for damage detection of fiber reinforced polymer-wrapped concrete structures, *J. Eng. Mech.*, **128** (2002), 172–183. https://doi.org/10.1061/(ASCE)0733-9399(2002)128:2(172)
8. B. Wang, Q. Zhang, W. Zhao, Fast concrete crack detection method via L2 sparse representation, *Electron. Lett.*, **54** (2018), 752–754. https://doi.org/10.1049/el.2018.0412
9. F. Delbary, K. Erhard, R. Kress, R. Potthast, J. Schulz, Inverse electromagnetic scattering in a two-layered medium with an application to mine detection, *Inverse Probl.*, **24** (2008), 015002. https://doi.org/10.1088/0266-5611/24/1/015002
10. P. Gao, L. Collins, P. M. Garber, N. Geng, L. Carin, Classification of landmine-like metal targets using wideband electromagnetic induction, *IEEE Trans. Geosci. Remote Sens.Sens.*, **38** (2000), 1352–1361. https://doi.org/10.1109/36.843029
11. M. Cheney, A mathematical tutorial on synthetic aperture radar, *SIAM Rev.*, **43** (2001), 301–312. https://doi.org/10.1137/S0036144500368859

12. V. S. Chernyak, *Fundamentals of Multisite Radar Systems: Multistatic Radars and Multiradar Systems*, CRC Press, Routledge, 1998.

13. J. Garnier, K. Sølna, Coherent interferometric imaging for synthetic aperture radar in the presence of noise, *Inverse Probl.*, **24** (2008), 055001. https://doi.org/10.1088/0266-5611/24/5/055001

14. Y. Á. López, M. García-Fernández, G. Álvarez-Narciandi, F. L. H. Andrés, Unmanned aerial vehicle-based ground-penetrating radar systems: A review, *IEEE Geosci. Remote Sens. Mag.*, **10** (2022), 66–86. https://doi.org/10.1109/MGRS.2022.3160664

15. X. Liu, M. Serhir, M. Lambert, Detectability of underground electrical cables junction with a ground penetrating radar: electromagnetic simulation and experimental measurements, *Constr. Build. Mater.*, **158** (2018), 1099–1110. https://doi.org/10.1016/j.conbuildmat.2017.10.038

16. J. Jeong, W.-K. Park, S.-H. Son, Object localization in highly cluttered environments using neural network learning on microwave scattering data, *Microw. Opt. Technol. Lett.*, **66** (2024), e70020. https://doi.org/10.1002/mop.70020

17. J. Jin, F. Feng, W. Na, S. Yan, W. Liu, L. Zhu, et al., Recent advances in neural network-based inverse modeling techniques for microwave applications, *Int. J. Numer. Model.: Electron. Netw. Devices Fields*, **33** (2020), e2732. https://doi.org/10.1002/jnm.2732

18. P. Meng, Z. Xu, X. Wang, W. Yin, H. Liu, A novel method for solving the inverse spectral problem with incomplete data, *J. Comput. Appl. Math.*, **463** (2025), 116525. https://doi.org/10.1016/j.cam.2025.116525

19. W. Yin, Z. Shen, P. Meng, H. Liu, An online interactive physics-informed adversarial network for solving mean field games, *Eng. Anal. Bound. Elem.*, **169** (2024), 106002. https://doi.org/10.1016/j.enganabound.2024.106002

20. O. Kwon, J. K. Seo, J.-R. Yoon, A real-time algorithm for the location search of discontinuous conductivities with one measurement, *Comm. Pur. Appl. Math.*, **55** (2002), 1–29. https://doi.org/10.1002/cpa.3009

21. W.-K. Park, D. Lesselier, Reconstruction of thin electromagnetic inclusions by a level set method, *Inverse Probl.*, **25** (2009), 085010. https://doi.org/10.1088/0266-5611/25/8/085010

22. L. Jofre, A. Broquetas, J. Romeu, S. Blanch, A. P. Toda, X. Fabregas, et al., UWB tomographic radar imaging of penetrable and impenetrable objects, *Proc. IEEE*, **97** (2009), 451–464. https://doi.org/10.1109/JPROC.2008.2008854

23. S. Kang, W.-K. Park, A novel study on the bifocusing method in two-dimensional inverse scattering problem, *AIMS Math.*, **8** (2023), 27080–27112. https://doi.org/10.3934/math.20231386

24. S.-H. Son, W.-K. Park, Application of the bifocusing method in microwave imaging without background information, *J. Korean Soc. Ind. Appl. Math.*, **27** (2023), 109–122.

25. C. Y. Ahn, T. Ha, W.-K. Park, Direct sampling method for identifying magnetic inhomogeneities in limited-aperture inverse scattering problem, *Comput. Math. Appl.*, **80** (2020), 2811–2829. https://doi.org/10.1016/j.camwa.2020.10.009

26. K. Ito, B. Jin, J. Zou, A direct sampling method to an inverse medium scattering problem, *Inverse Probl.*, **28** (2012), 025003. https://doi.org/10.1088/0266-5611/28/2/025003

27. S. Kang, M. Lambert, C. Y. Ahn, T. Ha, W.-K. Park, Single- and multi-frequency direct sampling methods in limited-aperture inverse scattering problem, *IEEE Access*, **8** (2020), 121637–121649. https://doi.org/10.1109/ACCESS.2020.3006341

28. J. Guo, G. Yan, J. Jin, J. Hu, The factorization method for cracks in inhomogeneous media, *Appl. Math.*, **62** (2017), 509–533. https://doi.org/10.21136/AM.2017.0194-16

29. K. H. Leem, J. Liu, G. Pelekanos, An extended direct factorization method for inverse scattering with limited aperture data, *Inverse Probl. Sci. Eng.*, **28** (2020), 754–776. https://doi.org/10.1080/17415977.2019.1647195

30. J. Yang, B. Zhang, H. Zhang, The factorization method for reconstructing a penetrable obstacle with unknown buried objects, *SIAM J. Appl. Math.*, **73** (2012), 617–635. https://doi.org/10.1137/120883724

31. W.-K. Park, Asymptotic properties of MUSIC-type imaging in two-dimensional inverse scattering from thin electromagnetic inclusions, *SIAM J. Appl. Math.*, **75** (2015), 209–228. https://doi.org/10.1137/140975176

32. W.-K. Park, Application of MUSIC algorithm in real-world microwave imaging of unknown anomalies from scattering matrix, *Mech. Syst. Signal Proc.*, **153** (2021), 107501. https://doi.org/10.1016/j.ymssp.2020.107501

33. Y. Zhong, X. Chen, MUSIC imaging and electromagnetic inverse scattering of multiple-scattering small anisotropic spheres, *IEEE Trans. Antennas Propag.*, **55** (2007), 3542–3549. https://doi.org/10.1109/TAP.2007.910488

34. H. Ammari, J. Garnier, H. Kang, W.-K. Park, K. Sølna, Imaging schemes for perfectly conducting cracks, *SIAM J. Appl. Math.*, **71** (2011), 68–91. https://doi.org/10.1137/100800130

35. W.-K. Park, Real-time microwave imaging of unknown anomalies via scattering matrix, *Mech. Syst. Signal Proc.*, **118** (2019), 658–674. https://doi.org/10.1016/j.ymssp.2018.09.012

36. W.-K. Park, On the identification of small anomaly in microwave imaging without homogeneous background information, *AIMS Math.*, **8** (2023), 27210–27226. https://doi.org/10.3934/math.20231392

37. J. F. Funes, J. M. Perales, M.-L. Rapún, J. M. Vega, Defect detection from multi-frequency limited data via topological sensitivity, *J. Math. Imaging Vis.*, **55** (2016), 19–35. https://doi.org/10.1007/s10851-015-0611-y

38. F. L. Louër, M.-L. Rapún, Topological sensitivity for solving inverse multiple scattering problems in 3D electromagnetism. Part I: one step method, *SIAM J. Imag. Sci.*, **10** (2017), 1291–1321. https://doi.org/10.1137/17M1113850

39. W.-K. Park, Performance analysis of multi-frequency topological derivative for reconstructing perfectly conducting cracks, *J. Comput. Phys.*, **335** (2017), 865–884. https://doi.org/10.1016/j.jcp.2017.02.007

40. R. Potthast, A study on orthogonality sampling, *Inverse Probl.*, **26** (2010), 074015. https://doi.org/10.1088/0266-5611/26/7/074015

41. R. Griesmaier, Multi-frequency orthogonality sampling for inverse obstacle scattering problems, *Inverse Probl.*, **27** (2011), 085005. https://doi.org/10.1088/0266-5611/27/8/085005

42. C. Y. Ahn, S. Chae, W.-K. Park, Fast identification of short, sound-soft open arcs by the orthogonality sampling method in the limited-aperture inverse scattering problem, *Appl. Math. Lett.*, **109** (2020), 106556. https://doi.org/10.1016/j.aml.2020.106556

43. I. Harris, D.-L. Nguyen, Orthogonality sampling method for the electromagnetic inverse scattering problem, *SIAM J. Sci. Comput.*, **42** (2020), B722–B737. https://doi.org/10.1137/19M129783X

44. M. T. Bevacqua, T. Isernia, R. Palmeri, M. N. Akinci, L. Crocco, Physical insight unveils new imaging capabilities of orthogonality sampling method, *IEEE Trans. Antennas Propag.*, **68** (2020), 4014–4021. https://doi.org/10.1109/TAP.2019.2963229

45. T. Le, D.-L. Nguyen, H. Schmidt, T. Truong, Imaging of 3D objects with experimental data using orthogonality sampling methods, *Inverse Probl.*, **38** (2021), 025007. https://doi.org/10.1088/1361-6420/ac3d85

46. K. Belkebir, M. Saillard, Special section: Testing inversion algorithms against experimental data, *Inverse Probl.*, **17** (2001), 1565–1571. https://doi.org/10.1088/0266-5611/17/6/301

47. J.-M. Geffrin, P. Sabouroux, C. Eyraud, Free space experimental scattering database continuation: experimental set-up and measurement precision, *Inverse Probl.*, **21** (2005), S117–S130. https://doi.org/10.1088/0266-5611/21/6/S09

48. D. M. Pozar, *Microwave Engineering*, 4th edition, John Wiley & Sons, Inc., 2011.

49. D. Colton, R. Kress, Inverse Acoustic and Electromagnetic Scattering Problems, In: *Mathematics and Applications Series,* Springer, New York, 1998. https://doi.org/10.1007/978-3-662-03537-5

50. N. Bleistein, J. W. Stockwell, J. K. Cohen, Mathematics of Multidimensional Seismic Imaging, Migration, and Inversion, In: *Interdisciplinary Applied Mathematics,* Springer, New York, 2001. https://doi.org/10.1007/978-1-4613-0001-4

51. M. Slaney, A. C. Kak, L. E. Larsen, Limitations of imaging with first-order diffraction tomography, *IEEE Trans. Microw. Theory Techn.*, **32** (1984), 860–874. https://doi.org/10.1109/TMTT.1984.1132783

52. S. Hou, K. Sølna, H. Zhao, A direct imaging algorithm for extended targets, *Inverse Probl.*, **22** (2006), 1151–1178. https://doi.org/10.1088/0266-5611/22/4/003

53. R. Solimene, A. Cuccaro, G. Ruvio, D. F. Tapia, M. O'Halloran, Beamforming and holography image formation methods: an analytic study, *Opt. Express*, **24** (2016), 9077–9093. https://doi.org/10.1364/OE.24.009077

54. S. Kang, S. Chae, W.-K. Park, A study on the orthogonality sampling method corresponding to the observation directions configuration, *Res. Phys.*, **33** (2022), 105108. https://doi.org/10.1016/j.rinp.2021.105108

55. I. Harris, D.-L. Nguyen, T.-P. Nguyen, Direct sampling methods for isotropic and anisotropic scatterers with point source measurements, *Inverse Probl. Imag.*, **16** (2022), 1137–1162. https://doi.org/10.3934/ipi.2022015

56. M. Abramowitz, I. A. Stegun, *Handbook of Mathematical Functions, with Formulas, Graphs, and Mathematical Tables*, Dover, New York, 1996.

57. W.-K. Park, Multi-frequency subspace migration for imaging of perfectly conducting, arc-like cracks in full- and limited-view inverse scattering problems, *J. Comput. Phys.*, **283** (2015), 52–80. https://doi.org/10.1016/j.jcp.2014.11.036

58. A. Carpio, M. Pena, M.-L. Rapún, Processing the 2D and 3D Fresnel experimental databases via topological derivative methods, *Inverse Probl.*, **37** (2021), 105012. https://doi.org/10.1088/1361-6420/ac21c8

59. R. Marklein, K. Balasubramanian, A. Qing, K. J. Langenberg, Linear and nonlinear iterative scalar inversion of multi-frequency multi-bistatic experimental electromagnetic scattering data, *Inverse Probl.*, **17** (2001), 1597–1610. https://doi.org/10.1088/0266-5611/17/6/304

60. H. Ammari, J. Garnier, W. Jing, H. Kang, M. Lim, K. Sølna, et al., Mathematical and statistical methods for multistatic imaging, In: *Lecture Notes in Mathematics,* Springer, Cham, 2013. https://doi.org/10.1007/978-3-319-02585-8

61. W.-K. Park, Real-time detection of small anomaly from limited-aperture measurements in real-world microwave imaging, *Mech. Syst. Signal Proc.*, **171** (2022), 108937. https://doi.org/10.1016/j.ymssp.2022.108937

62. C. Y. Ahn, S. Chae, S. Kang, K.-J. Lee, W.-K. Park, S.-H. Son, Orthogonality sampling method for identifying small anomalies in real-world microwave imaging, *East Asian J. Appl. Math.*, **14** (2024), 293–313. https://doi.org/10.4208/eajam.2022-318.170723

63. W.-K. Park, On the application of orthogonality sampling method for object detection in microwave imaging, *IEEE Trans. Antennas Propag.*, **71** (2023), 934–946. https://doi.org/10.1109/TAP.2022.3220033

64. P. Jaccard, The distribution of the flora in the alpine zone, *New Phytol.*, **11** (1912), 37–50. https://doi.org/10.1111/j.1469-8137.1912.tb05611.x

65. J.-M. Geffrin, P. Sabouroux, Continuing with the Fresnel database: experimental setup and improvements in 3D scattering measurements, *Inverse Probl.*, **25** (2009), 024001. https://doi.org/10.1088/0266-5611/25/2/024001

66. C. Geng, M. Song, X. Wang, Y. Wang, Time-domain direct sampling method for inverse electromagnetic scattering with a single incident source, *SIAM J. Imag. Sci.*, **18** (2025), 1208–1234. https://doi.org/10.1137/24M1701071

67. Y. Guo, H. Li, X. Wang, A novel time-domain direct sampling approach for inverse scattering problems in acoustics, *SIAM J. Appl. Math.*, **84** (2024), 2152–2174. https://doi.org/10.1137/23M1622854

AIMS Press